An integrated model for three-dimensional cohesive sediment transport in storm event and its application on Lianyungang Harbor, China

Xiaochen Yang · Qinghe Zhang · Jinfeng Zhang ·
Feng Tan · Yuru Wu · Na Zhang · Hua Yang · Qixiu Pang

Abstract Prediction of cohesive sediment transport in storm process is important for both navigation safety and environment of the coastal zone. The difficulties to simulate cohesive sediment transport for a small-scale area such as around a harbor during storm events mainly include the low spatial resolution of the present reanalysis atmosphere forcing, the complex hydrodynamic and sediment transport processes, and their interactions. In this paper, an integrated atmosphere-wave-3D hydrodynamic and cohesive sediment transport model with unstructured grid, which is comprised of the Weather Research and Forecasting (WRF) model, Simulating WAves Nearshore (SWAN) model, and Finite-Volume Coastal Ocean Model (FVCOM), was developed to solve the abovementioned problems. For cohesive sediment, the flocculation and hindered settling were included, and a self-weight consolidation processes was introduced to the existing FVCOM. Interactions between components were considered by providing data fields to each other in an offline manner. The integrated model was applied to simulate cohesive sediment transport around Lianyungang Harbor, China, during Typhoon Wipha in 2007. Results identify that the atmosphere model WRF performed better in the simulation of wind field during typhoon process compared with QuikSCAT/National Centers for Environmental Prediction (QSCAT/NCEP) data. Simulation of wave model was directly affected by wind results as wave vector field driven by WRF wind field showed anticlockwise vortex while waves driven by QSCAT/NCEP wind field did not. The influence of water elevation and flow field on waves was great at the nearshore area. However, the effect of wave on current was not apparent, while the wind field played a more important role, especially on the current velocity. The cohesive sediment transport was greatly affected by wave due to the combined wave-current-induced shear stress. In general, simulation results of wind, wave, current, and sediment showed reasonable agreement with measured data. It is demonstrated that the integrated model developed in the paper is capable of providing high-resolution atmosphere data for other components, reproducing the complex hydrodynamics and cohesive sediment transport processes and taking account of the interaction between components. The integrated model is necessary for simulating the cohesive sediment transport in a small-scale area during storm events.

Keywords Storm · Integrated model · WRF · SWAN · FVCOM · Cohesive sediment transport

X. Yang
Research Institute of Water Resources and Hydropower, Liaoning Province, Shenyang 110003, Liaoning Province, China

Q. Zhang (✉) · J. Zhang · F. Tan · Y. Wu
State Key Laboratory of Hydraulic Engineering Simulation and Safety, Tianjin University, 300072 Tianjin, China
e-mail: qhzhang@tju.edu.cn

N. Zhang · H. Yang · Q. Pang
Key Laboratory of Engineering Sediment, Ministry of Transport, Tianjin Research Institute of Water Transport Engineering, 300456 Tianjin, China

1 Introduction

Storm processes such as typhoon and extratropical storm usually induce strong waves and complex currents in nearshore zone and exert great impacts on cohesive sediment transport on muddy coast. The cohesive sediment transport in storm events not only causes strong siltation in entrance channels

that threatens the navigation safety but also affects the coastal environment because the fine sediment adsorbs and spreads contaminants. Therefore, it is of great importance to predict cohesive sediment transport during storm processes.

In recent years, the cohesive sediment transport during storm events has been extensively studied by using 3D numerical models. Some models such as MOHID (Neves 2003; Zhang 2004) and EFDC (Hamrick 1992; Gong and Shen 2009; Liu and Huang 2009) are capable of simulating cohesive sediment transport affected by waves and currents during storm processes. However, it is difficult to develop a realistic cohesive sediment transport model for a small-scale harbor in storm events, because the factors of wind, wave, and current processes are all prerequisite and need to be described accurately enough to reproduce the physical processes. The main difficulties for simulating cohesive sediment transport during storm events lay in three aspects. First, the spatial resolution of present reanalysis atmosphere data obtained is too low to describe the variation of storm wind fields. For example, the spatial and temporal resolutions of QuikSCAT/National Centers for Environmental Prediction (QSCAT/NCEP) reanalysis data are 0.5° and 6 h, both are too coarse, with some harbors only covering an area of 1°×1°. To solve this problem, previous studies used the Weather Research and Forecasting (WRF) model to obtain high-resolution atmosphere forces, for example, Gu et al. (2005) used the WRF model to simulate Typhoon Rusa (2002) with a horizontal resolution of 10 km and time step of 30 s. Observation data was assimilated into the model through 3D-var data assimilation. The good performance of WRF and the high-resolution results demonstrates that it is necessary to employ WRF model for simulating the wind fields during the storms. The second difficulty is the complex hydrodynamic and sediment transport processes and their interaction during storm events. To achieve this, we should employ nearshore wave and hydrodynamic and sediment models and establish the exchange of data fields to each other to include interactions. And the last is about the complexity of the properties of the cohesive sediments. This has been investigated by various researchers (Dankers and Winterwerp 2007; Sanford 2008; Xie et al. 2010) and we will mainly refer to previous researches in our study.

Integrated and coupling models with proper component models cannot only obtain reasonable results of a single factor but also take account of the interaction between each component. Therefore, integrated and coupling models become necessary for simulation of cohesive sediment transport in storm events. Warner et al. (2008b) developed a 3D coupled wave, current, and sediment transport model based on the ROMS model, and this coupled model was applied to simulate storm-driven sediment transport in Massachusetts Bay (Warner et al. 2008a). Zhao (2008) developed a 3D integrated model consisting of a cyclone model (Holland 1980), Simulating WAves Nearshore (SWAN) model, and

ECOMSED model to simulate cohesive sediment siltation in storm events. Most recently, Warner et al. (2010) developed a coupled ocean-atmosphere-wave-sediment transport (COAWST) modeling system in structured grid and applied in the simulation of Hurricane Isabel. The coupled model was applied to investigate ocean-atmosphere-wave interaction during Hurricane Ida and Nor'Ida (Olabarrieta et al. 2012). However, most of the above studies used structured grid and did not focus on cohesive sediment transport. It is anticipated that the unstructured grid is more flexible to follow the irregular coastlines, and more complicated processes concentrating on cohesive sediment should be included in the model.

In the present paper, we have developed an integrated atmosphere-wave-3D hydrodynamic and cohesive sediment transport model with unstructured grid based on the WRF model, SWAN model, and Finite-Volume Coastal Ocean Model (FVCOM). The data fields were exchanged offline among the components to include the coupling effects. The flocculation and hindered settling processes for cohesive sediment were included, and a consolidation model was introduced into the existing sediment model of FVCOM. Cohesive sediment transport was simulated with the influence of winds, waves, and currents. The integrated model was applied to investigate the coastal dynamic processes and channel siltation in the muddy coast, Lianyungang Harbor, China, during Typhoon Wipha in 2007. The paper is organized as follows: the model components and the model operation are described in Section 2. In Section 3, the application results and discussion are presented. The conclusions are demonstrated in Section 4.

2 Integrated model of cohesive sediment transport

The integrated model for description of cohesive sediment transport in storm event is comprised of four components as the atmosphere model WRF, the wave model SWAN, the hydrodynamic model FVCOM, and sediment model based on FVCOM. The atmosphere model WRF provides the wind field for wave simulation and hydrodynamic simulation, the SWAN wave model gives the wave field and radiation stress field for the hydrodynamic and sediment simulation of FVCOM, while FVCOM also returns water elevation and flow field for the wave simulation of the SWAN model. The individual components and the operation of the integrated model are described in the succeeding subsections.

2.1 Atmosphere model

The atmosphere model is the WRF model (Skamarock et al. 2008). WRF is a nonhydrostatic, fully compressible mesoscale numerical weather prediction system.

The atmosphere model integrates the compressible, nonhydrostatic, flux-form Euler equations. It utilizes

Arakawa-C grid in the horizontal and a terrain-following hydrostatic pressure coordinate (Laprise 1992) in the vertical. WRF is suitable for both operational forecasting and atmospheric research across scales ranging from meters to thousands of kilometers to predict 3D atmospheric variables including wind speed, surface pressure, air temperature, precipitation, humidity, longwave and shortwave radiation, and heat flux. More details about the WRF model can be found in Skamarock et al. (2008) and Wang et al. (2011). In recent years, WRF has been employed to predict atmosphere parameters during hurricanes or typhoons (Gu et al. 2005; Rosenfeld et al. 2007; Chen et al. 2010). It is demonstrated that WRF has shown good performance in the prediction of hurricane tracks and intensity.

2.2 Wave model

For the wave model, we use the SWAN model. SWAN is a third-generation wave model developed by Delft University that computes random, short-crested wind-generated waves in shallow water. It solves the action balance equation with sources and sinks (Booij et al. 1999):

$$\frac{\partial N}{\partial t} + \frac{\partial c_x N}{\partial x} + \frac{\partial c_y N}{\partial y} + \frac{\partial c_\sigma N}{\partial \sigma_r} + \frac{\partial c_\theta N}{\partial \theta} = \frac{S}{\sigma_r} \tag{1}$$

where N represents the wave action density, the first term on the left-hand side is the change of action density in time, the second and third terms represent the propagation of action density in geographical space (with c_x and c_y the propagation velocities in x and y directions), the fourth term represents the change of relative radiation frequency σ_r due to variations in depths and currents (with propagation velocity c_σ in frequency space), and the fifth term is depth-induced and current-induced refraction (with θ the direction normal to the wave crest and c_θ the propagation velocity in directional space). The term on the right-hand side represents the source and sinks of energy density including the transfer of wind energy to the waves, the dissipation of wave energy due to whitechapping, the dissipation of wave energy due to bottom friction, quadruplet and triad wave-wave interaction, and depth-induced breaking.

Zijlema (2010) presented the unstructured mesh instead of the structured version of SWAN with a vertex-based, fully implicit, finite difference method. The unstructured grid SWAN model retains the physics and numerics of the structured version and has been validated by idealized and realistic cases. Here the unstructured grid SWAN is used.

2.3 Hydrodynamic model

For the 3D hydrodynamic model, FVCOM is employed. FVCOM is a 3D unstructured grid, free-surface primitive equation ocean model (Chen et al. 2003, 2004).

The governing equations of FVCOM consist of momentum, continuity, temperature, salinity, and density equations. FVCOM uses the triangular grids in the horizontal and sigma coordinate transformation in the vertical. The horizontal diffusion for the momentum is mathematically closed by the Smagorinsky parameterization method (Smagorinsky 1963). The vertical eddy mixing is closed by either the updated version of the Mellor-Yamada level 2.5 (Mellor and Yamada 1982; Mellor and Blumberg 2004) or turbulence closure models provided by the General Ocean Turbulent Model (GOTM) (Burchard, 2002). FVCOM employs a "mode splitting" method with the sea surface elevation computed by solving the vertical averaged equations using a smaller time step (external mode) and the 3D equations solved with given free surface using a larger time step (internal mode).

The influence of wave is included by adding the radiation stress terms to the momentum equations based on Mellor (2003, 2005). The horizontal radiation terms (S_{xx}, S_{xy}, S_{yx}, and S_{yy}) and vertical radiation terms (S_{px} and S_{py}) are shown as follows:

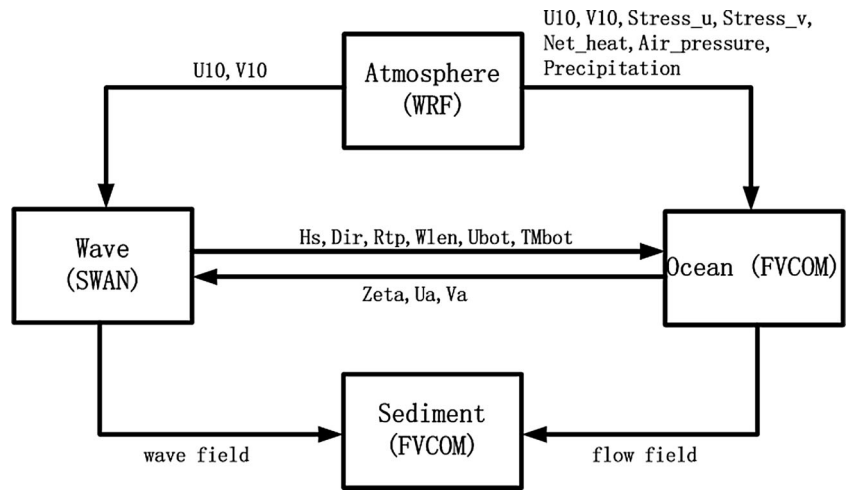$$S_{xx} = k_w E \left(\frac{k_x k_x}{k_w^2} F_{CS} F_{CC} + F_{CS} F_{CC} - F_{SS} F_{SC} \right) + \frac{k_x k_x}{k_w} \frac{c^2}{L} A_R R_z \tag{2}$$

$$S_{xy} = S_{yx} = k_w E \left(\frac{k_x k_y}{k_w^2} F_{CS} F_{CC} \right) + \frac{k_x k_y}{k_w} \frac{c^2}{L} A_R R_z \tag{3}$$

$$S_{yy} = k_w E \left(\frac{k_y k_y}{k_w^2} F_{CS} F_{CC} + F_{CS} F_{CC} - F_{SS} F_{SC} \right) + \frac{k_y k_y}{k_w} \frac{c^2}{L} A_R R_z \tag{4}$$

$$S_{px} = (F_{CC} - F_{SS}) \left[\frac{F_{SS}}{2} \frac{\partial E}{\partial x} + F_{CS} E (1+\sigma) \frac{\partial (k_w D)}{\partial x} - E F_{SS} \coth(k_w D) \frac{\partial (k_w D)}{\partial x} \right] \tag{5}$$

$$S_{py} = (F_{CC} - F_{SS}) \left[\frac{F_{SS}}{2} \frac{\partial E}{\partial y} + F_{CS} E (1+\sigma) \frac{\partial (k_w D)}{\partial y} - E F_{SS} \coth(k_w D) \frac{\partial (k_w D)}{\partial y} \right] \tag{6}$$

Fig. 1 Modeling scheme and data exchange of integrated model components

where k_w is the wave number, k_x and k_y are the wave-number components in the x and y directions, c is the wave propagation speed, L is the wave length, and D is the water depth. E is the wave energy and the vertical structure functions are computed as:

$$F_{CS} = \frac{\cosh[k_w D(1+\sigma_w)]}{\sinh(k_w D)}; \quad F_{CC} = \frac{\cosh[k_w D(1+\sigma_w)]}{\cosh(k_w D)}$$

$$F_{SS} = \frac{\sinh[k_w D(1+\sigma_w)]}{\sinh(k_w D)}; \quad F_{SC} = \frac{\sinh[k_w D(1+\sigma_w)]}{\cosh(k_w D)} \tag{7}$$

where $\sigma_w = 2\pi/T$ is the wave frequency, with T as the wave period. The last terms of Eqs. (2), (3), and (4) represent the

surface roller, with A_R as the roller area and R_z as the vertical distribution of the roller (Svendsen 1984):

$$A_R = \frac{\alpha}{\sqrt{2}} H_s L Q_b \tag{8}$$

$$R_z = 1 - \tanh\left(\frac{2\sigma}{\gamma}\right)^4 \tag{9}$$

where $\alpha=0.06$ is a parameter, H_s is the significant wave height, Q_b is the fraction of breaking waves, σ is the vertical sigma coordinate, and $\gamma = H_s/D$ is the ratio of wave height to water depth.

Fig. 2 Sketch map of the study
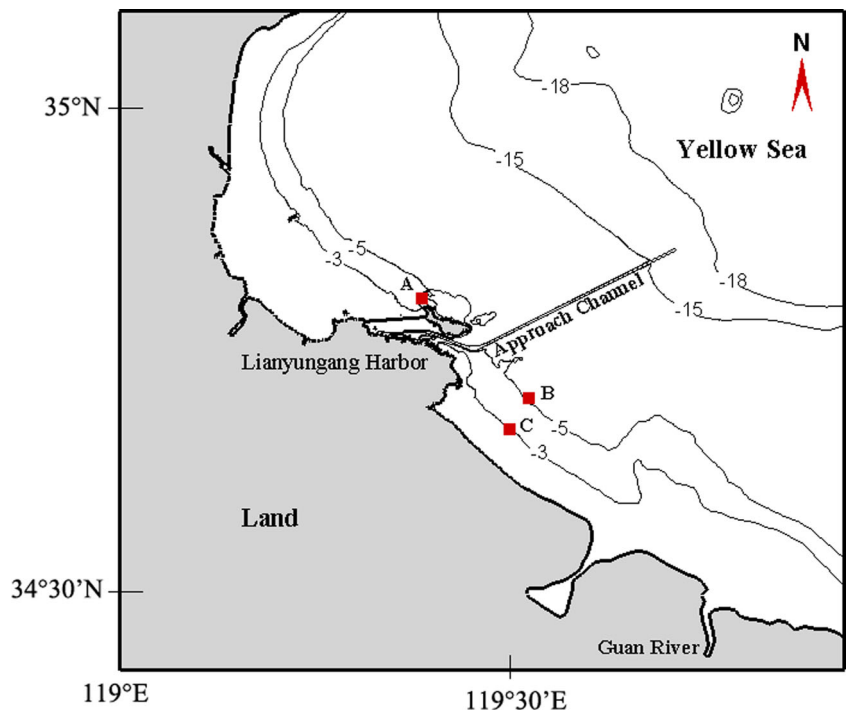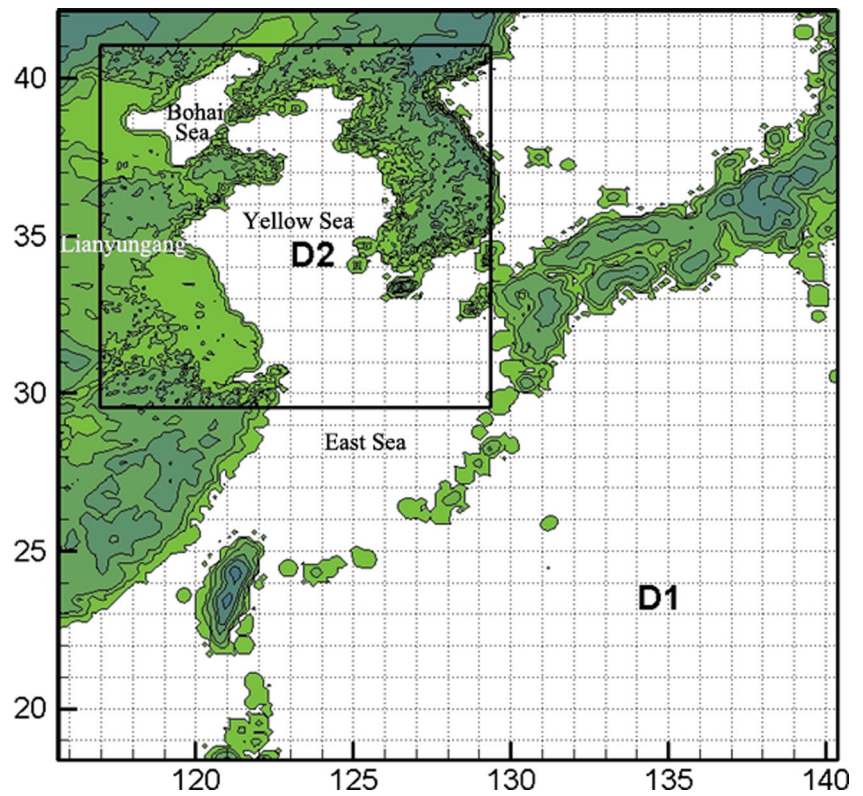area; locations of observation
stations

2.4 Sediment model

The sediment model is based on the Community Model for Coastal Sediment Transport (Warner et al 2008b) developed by the U. S. Geological Survey and other researchers. The module has been implemented into the FVCOM (Chen et al. 2003, 2004). For cohesive sediment transport, flocculation settling and hindered settling processes are included in the

Sub-domain   Large domain

Depth(m) -160 -150 -140 -130 -120 -110 -100 -90 -80 -70 -60 -50 -40 -30 -20 -10 0
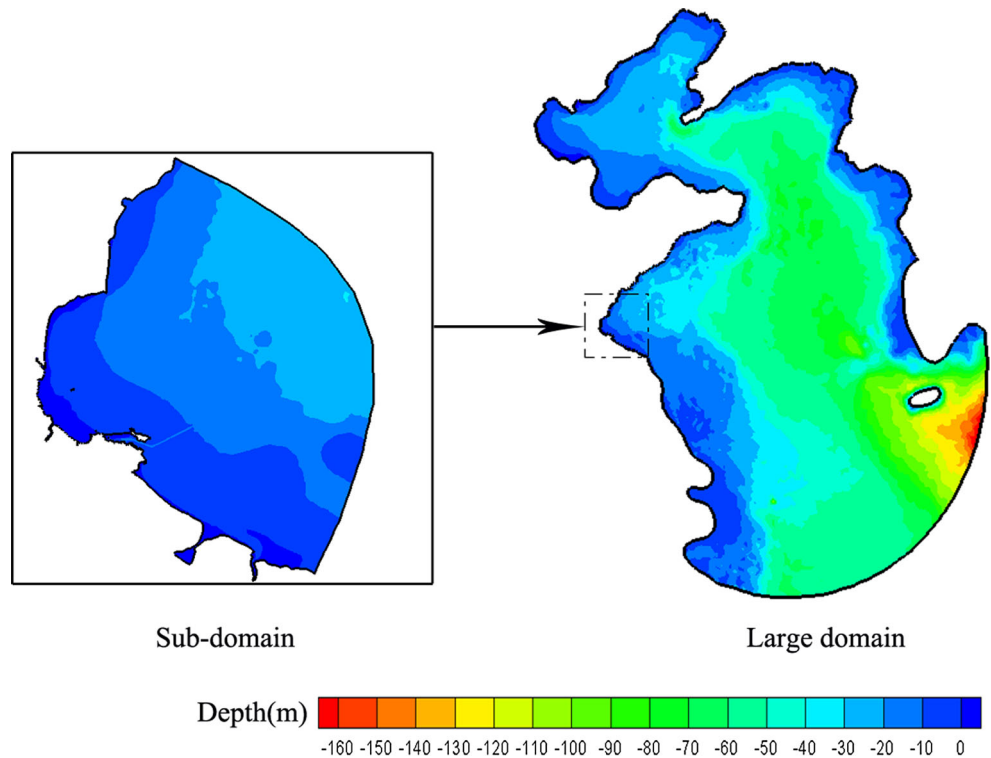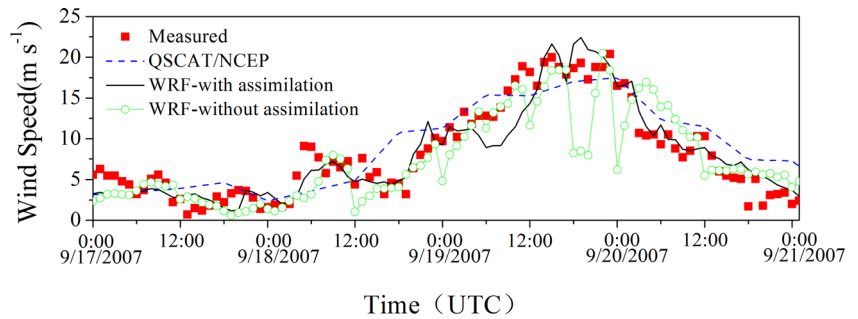
Fig. 5 Time series of wind speed for simulation of WRF with and without assimilation, QSCAT/NCEP data and measured data during Typhoon Wipha

model. For description of channel siltation, a first-order empirical consolidation expression is introduced into the existing model in the present paper.

The transport of suspended sediment is governed by the 3D advection-diffusion equation:

$$\frac{\partial(C)}{\partial t} + \frac{\partial(uC)}{\partial x} + \frac{\partial(vC)}{\partial y} + \frac{\partial((w-w_s)C)}{\partial z} = \frac{\partial}{\partial x}\left(A_H \frac{\partial C}{\partial x}\right)$$
$$+ \frac{\partial}{\partial y}\left(A_H \frac{\partial C}{\partial y}\right) + \frac{\partial}{\partial Z}\left(K_h \frac{\partial C}{\partial z}\right) \tag{10}$$

where C is the suspended sediment concentration; A_H is the horizontal eddy viscosity coefficient, and K_h is the vertical diffusion coefficient; u, v, and w are flow velocity components in x, y, and z directions; w_s is the sediment settling velocity.

The boundary conditions are set as follows:

The surface boundary condition is no-flux:

$$K_h \frac{\partial C}{\partial z} = 0 \tag{11}$$

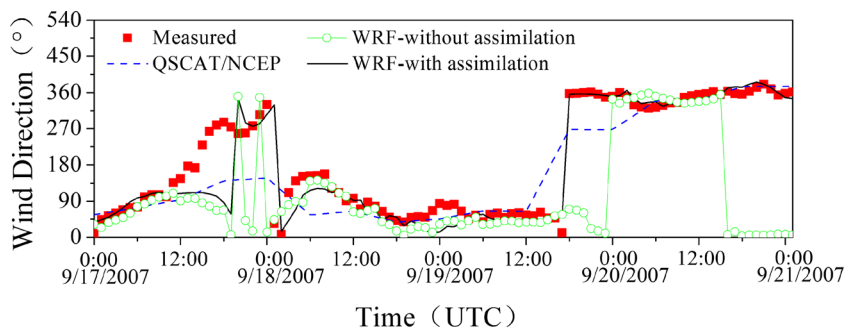At the bottom, the flux difference between erosion and deposition is imposed:

$$K_h \frac{\partial C}{\partial z} = F_E - F_D \tag{12}$$

where F_E and F_D are erosion flux and deposition flux, respectively. The erosion flux is calculated following the expression of Ariathurai and Arulanandan (1978) as:

$$F_E = E_0(1 - P_b)\left(\frac{\tau_b}{\tau_c} - 1\right), \quad \tau_b > \tau_e$$
$$F_E = 0, \quad \tau_b < \tau_e \tag{13}$$

where E_0 is the erosion rate and P_b is the porosity. τ_b is the bottom shear stress and τ_e is the critical shear stress for erosion. Deposition flux is calculated as:

$$F_D = w_s C, \quad \tau_b < \tau_d$$
$$F_D = 0, \quad \tau_b > \tau_d \tag{14}$$

where τ_d is the critical shear stress for deposition.

Siltation thickness is calculated as:

$$z_b = \int_0^T \frac{F}{\rho_s} dt \tag{15}$$

where F is the net flux in basins or channels, represented as $F = F_D - F_E$; γ_s is the bulk density; and T is the time duration.

The processes of flocculation and hindered settling for cohesive sediment are included to calculate the settling velocity as (van Rijn 2007):

$$w_s = \phi_{floc}\phi_{hs}w_0 \tag{16}$$

where ϕ_{floc} is the flocculation factor and ϕ_{hs} is the hindered settling factor; w_0 is the free settling velocity of a single sediment particle in the clear water calculated by the Stokes formulation:

$$w_0 = \frac{(\rho_s - \rho_w)gD_{s50}^2}{18\rho_w\nu} \tag{17}$$

with ρ_s the sediment density and ρ_w the density of the water; D_{s50} is the median particle diameter; ν is the kinematic viscosity coefficient.

Fig. 6 Time series of wind direction for simulation of WRF with and without assimilation, QSCAT/NCEP data and measured data during Typhoon Wipha

Table 1 Mean absolute error of atmosphere results

Item	Scenario	Mean absolute error
Wind speed	QSCAT/NCEP	2.61
	WRF—without assimilation	3.75
	WRF—assimilation	1.77
Wind direction	QSCAT/NCEP	51.53
	WRF—without assimilation	106.37
	WRF—assimilation	31.29

The flocculation factor ϕ_{floc} is proposed on the basis of the experimental data of the earlier research work (Thorn 1981; Vinzon and Mehta 2003; Shi and Zhou 2004) as follows:

$$\phi_{\text{floc}} = \left[4 + {}^{10}\log\left(2C/C_{\text{gel}}\right)\right]^{\alpha}, \quad C < C_{\text{HS}} \tag{18}$$

where C_{gel} is the gelling concentration; C_{HS} is the concentration for hindered settling; $\alpha = (D_{\text{sand}}/D_{\text{s}50}) - 1$ is a factor which depends on the ratio of D_{sand} ($D_{\text{sand}} = 62\,\mu\text{m}$) and $D_{\text{s}50}$, with a minimum value of 0 for $D_{\text{s}50} = 62\,\mu\text{m}$ and maximum value of 3 for $D_{\text{s}50} < 16\,\mu\text{m}$; ϕ_{floc} varies between 1 and 10.

The hindered settling factor ϕ_{hs} is represented by Dankers and Winterwerp (2007) as:

$$\phi_{\text{hs}} = \left(1 - C/C_{\text{gel}}\right)^{m}(1 - C)/\left(1 + 2.5C/C_{\text{gel}}\right), \quad C \geq C_{\text{HS}} \tag{19}$$

where m is the factor accounting for nonlinear effects.

The self-weight consolidation process of the soft mud is taken into account in the present model. A first-order empirical expression which assumes the solid volume concentration of the fluid mud approaching an equilibrium state, which is described as the state of sediment bed after long times without disturbance, is added into the existing model. The consolidation equation is written as (Sanford 2008):

$$\frac{\partial\phi_{\text{s}}}{\partial t} = r_{\text{c}}\left(\phi_{\text{seq}} - \phi_{\text{s}}\right)H\left(\phi_{\text{seq}} - \phi_{\text{s}}\right) - r_{\text{s}}\left(\phi_{\text{seq}} - \phi_{\text{s}}\right)H\left(\phi_{\text{s}} - \phi_{\text{seq}}\right) \tag{20}$$

where ϕ_{s} is the solid volume fraction, ϕ_{seq} is the equilibrium mud solids volume fraction, H is the Heaviside step function whose value is 1 for positive argument and 0 for negative argument, r_{c} and r_{s} are first-order consolidation and swelling rate, respectively. For duration of each hour, the newly deposited sediment in the channel is regarded as an independent layer to calculate the consolidation using Eq. (20). For each

Fig. 7 Comparison of simulated and observed tracks of Typhoon Wipha
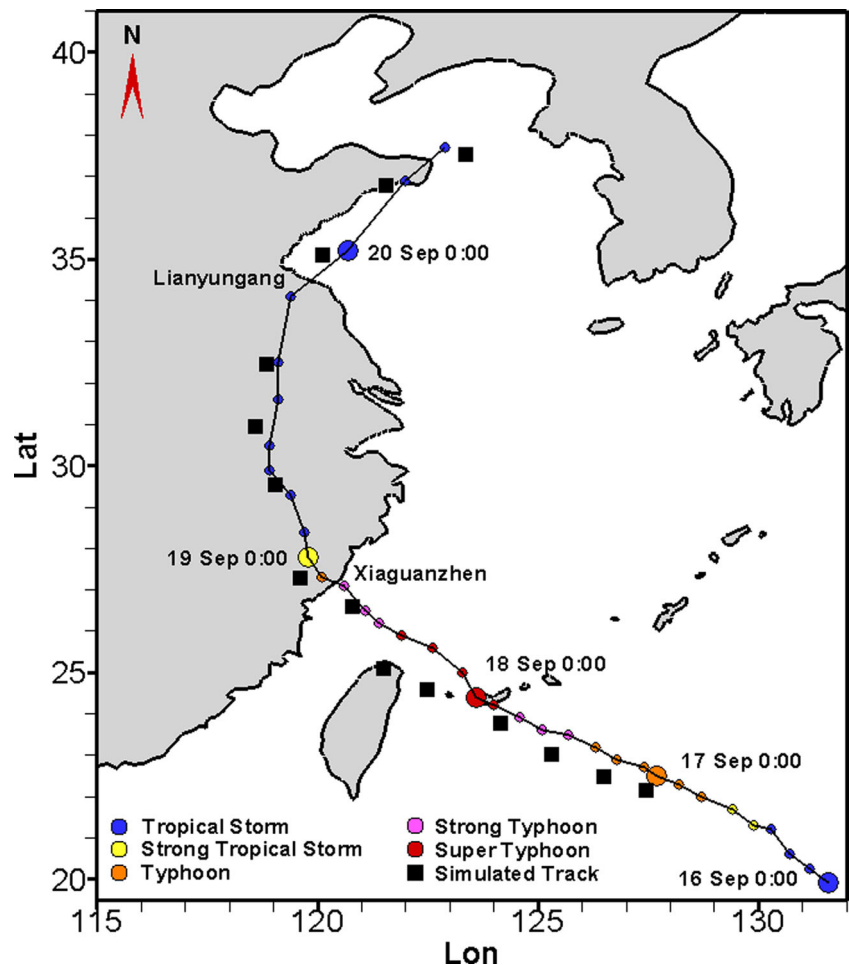
layer, the density of the mud increased from the initial state at the speed of r_c until it reached the equilibrium state. The surface density of each layer is assumed to equal to the bottom density of the layer that is above this layer to take account of the influence from the upper layer on the lower layer.

The bottom stress under combined wave and current condition is calculated by the bottom boundary layer model (Styles and Glenn 2000). Bottom stresses under pure currents τ_c and pure waves τ_w are initially estimated as follows, respectively:

$$\tau_c = \frac{(u^2 + v^2)\kappa^2}{\ln^2(z/z_0)} \tag{21}$$

$$\tau_w = 0.5 f_w u_b^2 \tag{22}$$

where $\kappa = 0.4$ is von Karman's constant, and z_0 is bottom roughness length. u_b represents the wave-orbital velocity amplitude and f_w is the wave friction factor which is given as:

$$f_w = \begin{cases} 0.3 & , \quad A_b/k_b \leq 0.2 \\ \exp\left(-8.82 + 7.02(A_b/k_b)^{-0.078}\right), & 0.2 < A_b/k_b \leq 100 \\ \exp\left(-7.30 + 5.61(A_b/k_b)^{-0.109}\right), & A_b/k_b > 100 \end{cases} \tag{23}$$

where A_b is the wave-orbital excursion amplitude and $k_b = 30z_0$. The bottom stresses under pure currents and pure waves are used as initial estimates for calculations toward consistent profiles for eddy viscosity and

Fig. 8 Comparison between wind fields of WRF simulation and QSCAT/NCEP data for the large domain at 18:00 of September 19th (UTC) and 12:00 of September 20th (UTC). The grid resolution of WRF model for the large domain was 15 km and the temporal resolution was 90 s. The wind field of WRF model was shown in every three grids for clarity
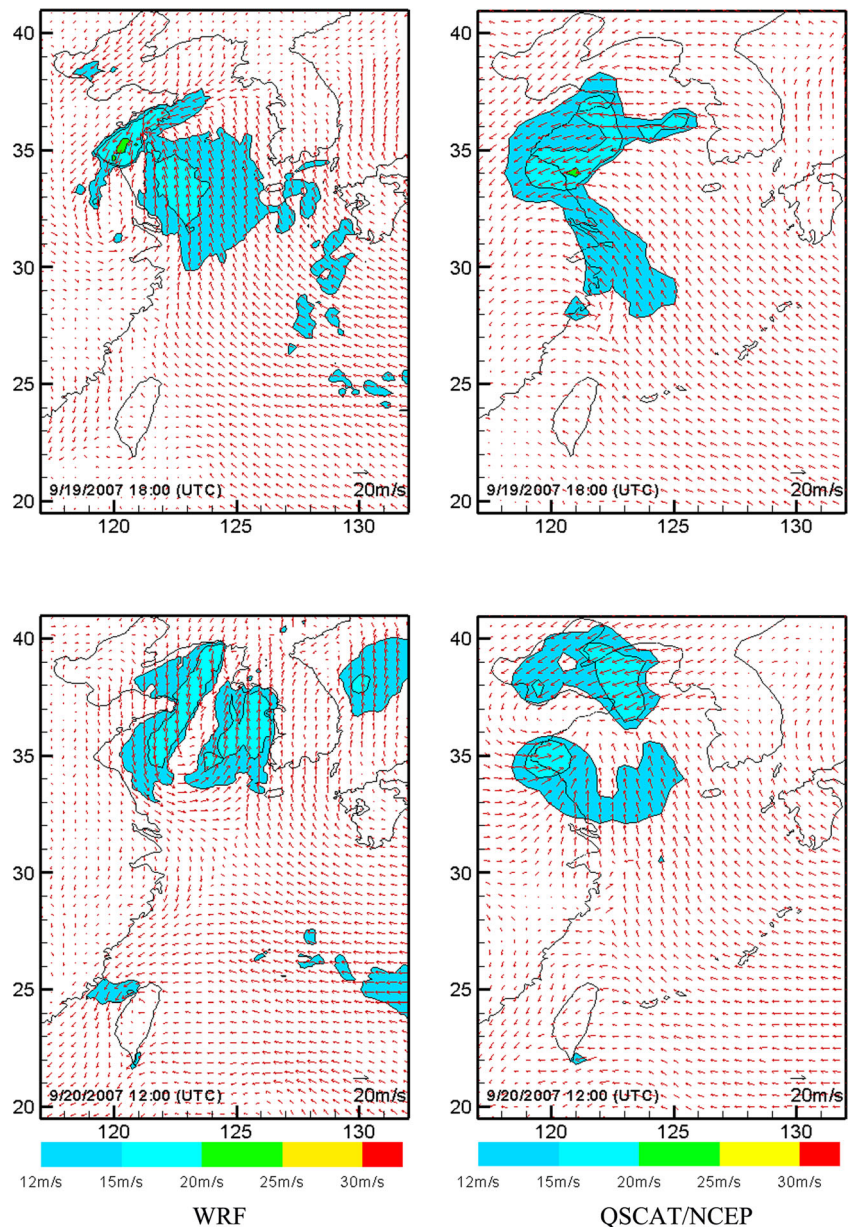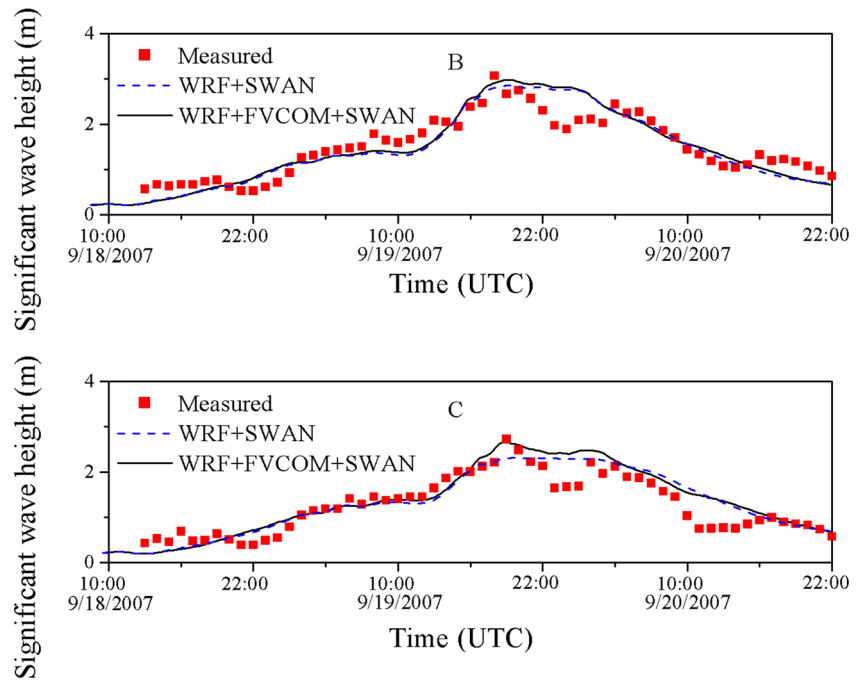
Fig. 9 Time series of significant wave heights for different model scenarios and the comparison with measured data during Typhoon Wipha (*panels B* and *C* are associated to measurement stations B and C)

velocity between z_0 and z_2 in the model calculated as (Styles and Glenn 2000):

$$K_{\mathrm{m}} = \begin{cases} \kappa u_{*\mathrm{c}} z & , & z > z_2 \\ \kappa u_{*\mathrm{wc}} z_1 & , & z_1 < z \le z_2 \\ \kappa u_{*\mathrm{wc}} z & , & z_0 \le z \le z_1 \end{cases} \qquad (24)$$

where K_{m} is eddy viscosity for momentum, z_1 defines the lower boundary of the transition layer, and $z_2 = z_1 u_{*\mathrm{wc}} / u_{*\mathrm{c}}$, with $u_{\rightarrow \mathrm{wc}} = \sqrt{\tau_{\mathrm{wc,max}}}$ and $u_{\rightarrow \mathrm{c}} = \sqrt{\tau_{\mathrm{c}}}$. $\tau_{\mathrm{wc,max}}$ is the

maximum bottom stress under combined currents and waves and defined as:

$$\tau_{\mathrm{wc,max}} = \sqrt{(\tau_{\mathrm{c}} + \tau_{\mathrm{w}} \cos\alpha)^2 + (\tau_{\mathrm{w}} \sin\alpha)^2} \qquad (25)$$

2.5 Model operation

The data exchange between model components is shown in Fig. 1. The atmosphere model simulates the wind field and

Fig. 10 Time series of mean wave periods for different model scenarios and the comparison with measured data during Typhoon Wipha (*panels B* and *C* are associated to measurement stations B and C)

Fig. 11 Time series of wave directions for different model scenarios and the comparison with measured data during Typhoon Wipha (*panels B and C* are associated to measurement stations B and C)
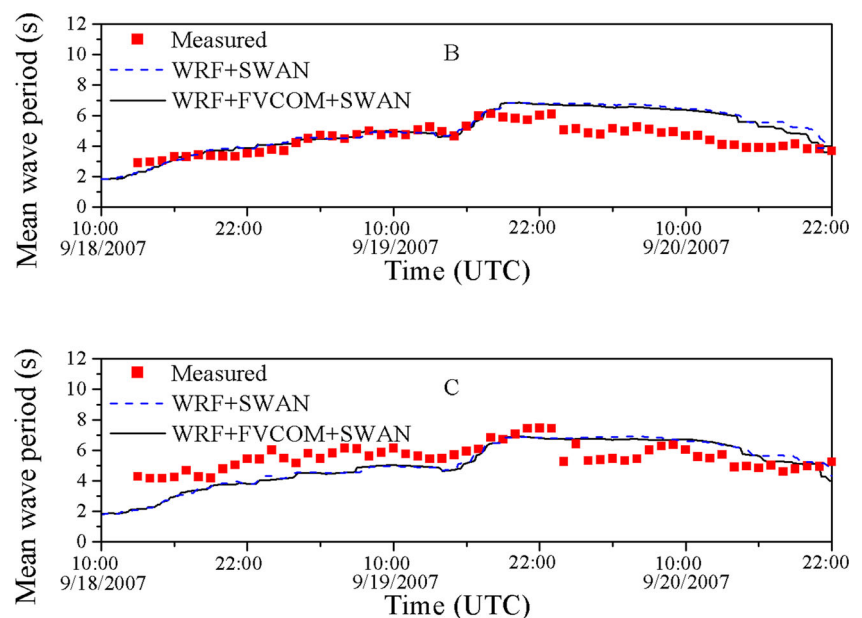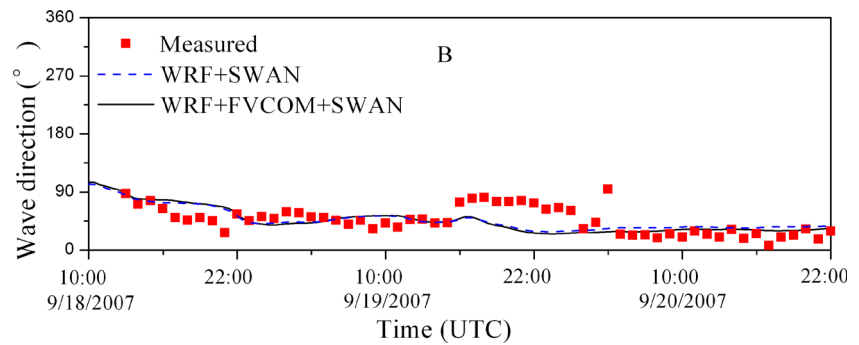

provides 10-m wind speed (U10, V10) to the wave model to compute wave parameters. It also provides 10-m wind speed (U10, V10), surface wind stress (Stress_u, Stress_v), heat fluxes (Net_heat), atmospheric pressure (Air_pressure), and precipitation (Precipitation) to the hydrodynamic model. Waves and currents are coupled in an offline way. The wave model provides the significant wave height (H_s), wave direction (Dir), peak wave period (Rtp), wave length (Wlen), bottom orbital velocity (Ubot), and bottom wave period (TMbot) to the hydrodynamic model. These parameters are used in hydrodynamic model to compute radiation stress for current. The spatial and time varying water elevation (Zeta) and vertical averaged current velocity (Ua, Va) are provided to the wave model to update the wave field by computing the current-induced refraction. The wave and current parameters are used to compute the bottom stress under the combined condition of waves and currents, which are provided to the sediment model to simulate sediment transport.

3 Application of the integrated model

3.1 Investigation area

Lianyungang Harbor (119° 27′ E, 34° 45′ N) locates on the east coast of China (Fig. 2). In the recent years, many researches on sediment properties around the harbor have been carried out, including field observations (Wang et al. 1980; Fan et al. 2009), laboratory experiments (Huang 1989), and numerical modeling (Xie et al. 2010). The coast around Lianyungang Harbor is a typical muddy coast because cohesive sediments with medium particle diameters from 2 to 4 μm are wildly distributed along the coast (Xie et al. 2010). The slope of the beach is very small, ranging from 1:1000 to 1:2000 (Chen et al. 1994).

Wipha is a strong typhoon which has threatened Chinese coastline in September 2007 which was formed out of a tropical disturbance at the northwest of Pacific Ocean on September 16th. It kept moving northwest and made landfall at Xiaguanzhen (120° 28′ E, 27° 10′ N) of Zhejiang Province, with a maximum wind speed of 45 ms^{-1}. Wipha passed Lianyungang from September 19th to 20th. Thereafter, it moved northeast and left Lianyungang Harbor and turned into

extratropical cyclone at north of Yellow Sea (http://www.wztf121.com/). The sketch of the track will be presented in Section 3.3.1 (see Fig. 7).

There is a permanent observation station, Da xishan station (A in Fig. 2) and two temporary observations (B and C in Fig. 2) near Lianyungang Harbor. The measurement data of wind was obtained from Station A. Station B (at water bathymetry contour of −5 m) and station C (at water bathymetry contour of −3 m) were established by Tianjin Research Institute of Water Transport Engineering, China, to carry out the field observation of Lianyungang Harbor during Typhoon Wipha. According to the observations, the maximum wind speed as the typhoon was passing was about 20.4 ms^{-1}, the maximum significant wave height reached 3 m, and the bottom sediment concentration was larger than 6 kg m^{-3}. There was a 150,000 deadweight ton (DWT) approach channel (Fig. 2) in Lianyungang Harbor. The siltation of the channel during Typhoon Wipha was also measured. The averaged siltation thickness in the approach channel was about 0.5 m and the maximum value reached 0.9 m. These extreme events might threaten the navigation of the harbor and channel, so it was important to investigate the cohesive sediment transport in the Lianyungang Harbor during storms.

Table 2 Mean absolute errors of wave results

Item	Scenario	Mean absolute error
Significant wave height (station B)	WRF+SWAN	0.25
	WRF+FVCOM+SWAN	0.26
Significant wave height (station C)	WRF+SWAN	0.22
	WRF+FVCOM+SWAN	0.23
Mean wave period (station B)	WRF+SWAN	0.86
	WRF+FVCOM+SWAN	0.76
Mean wave period (station C)	WRF+SWAN	0.98
	WRF+FVCOM+SWAN	0.94
Wave direction (station B)	WRF+SWAN	16.41
	WRF+FVCOM+SWAN	16.03

Fig. 12 Comparison of wave vector fields driven by WRF wind field and QSCAT/NCEP wind field at 19:00 of September 19th (UTC) and 13:00 of September 20th (UTC)
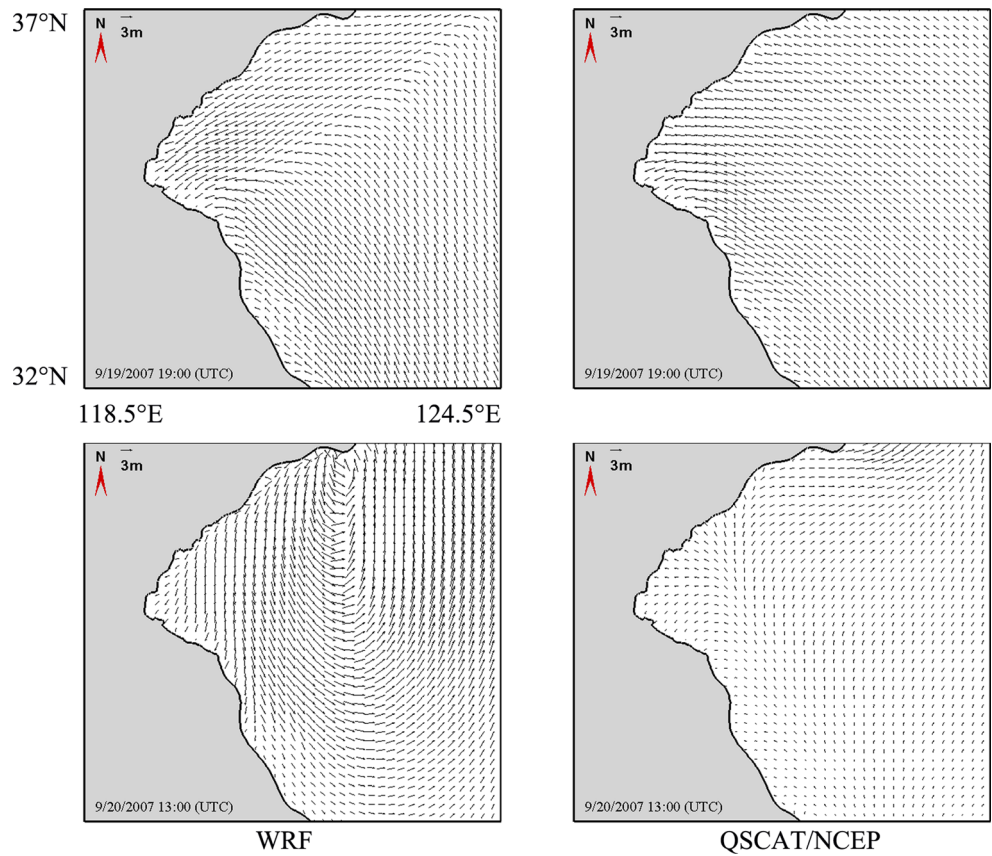
3.2 Model setup

3.2.1 WRF setup

Initial and time varying boundary conditions for the atmosphere model, mainly the fields of meteorological data and sea surface temperature (SST) data were obtained from the NCEP Final Analysis (FNL) Global Analysis 1 degree data (http://dss.ucar.edu/datasets/ds083.2/) with the temporal resolution of 6 h. WRF employed a data assimilation technique to ingest the observation data into the simulation. Here the three-dimensional (3D-Var) data assimilation was used. The observation data was obtained

from the NCEP ADP Global Upper Air and Surface Weather Observations which were composed of a global set of surface and upper air reports (http://dss.ucar.edu/datasets/ds337.0). WRF employed a two-way nested run with domains of different resolutions run simultaneously and communicate with each other (ARW; Skamarock et al. 2008). Two nesting domains, as shown in Fig. 3, were used, with the grid resolution of 15 km for the large domain (D1) and 5 km for the subdomain (D2). Thirty-four vertical sigma layers were used in the model. The modeling time steps for large domain and subdomain were 90 and 30 s, respectively. The 3D-var data assimilation was performed every 6 h.

Fig. 13 Comparison of significant wave height with and without the influence of tide during Typhoon Wipha at location with water depth of −1 m
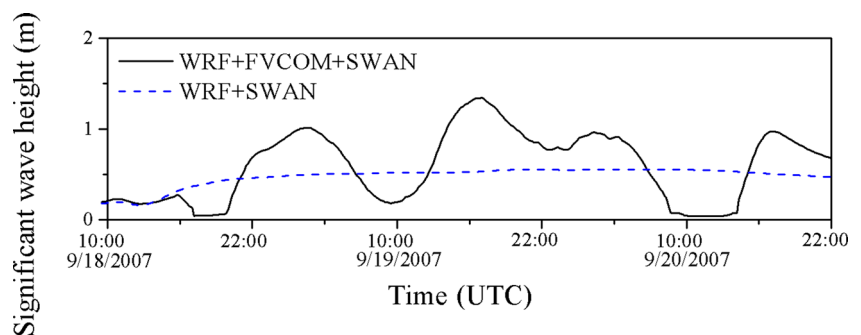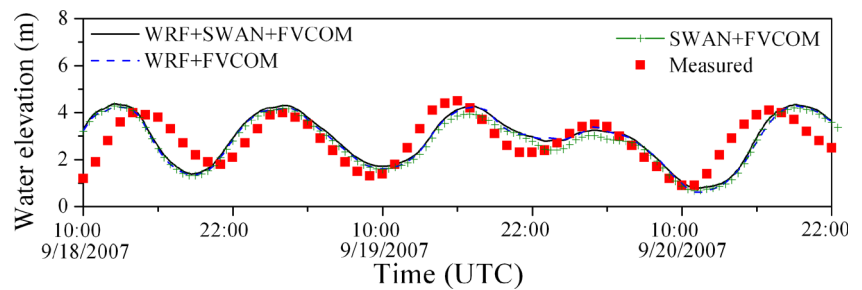
Fig. 14 Time series of simulated water elevations for different model scenarios and the comparison with measured data during Typhoon Wipha at station B

3.2.2 SWAN setup

The unstructured grid was employed for the wave model and two nesting domains (Fig. 4) were applied. Temporal and spatial varying 10-m wind speeds were obtained from the atmosphere model and interpolated to the grids of the wave model. The one-way nesting was used with the large model computing the wave spectra as the boundary condition of the subdomain. The grid sizes varied between 2000 and 125 m for the large domain and ranged from 1500 to 20 m for the subdomain. The time steps were both 5 min.

3.2.3 FVCOM setup for hydrodynamic simulation

The 3D hydrodynamic model used the same calculation domains as the wave model (Fig. 4). The boundary condition for the large domain was water elevation predicted by Chinatide (Li and Zheng 2007) which could give good time series

prediction of water elevation as the tide database and software in China seas. The simulated results of the large domain provided boundary condition for the subdomain. The FVCOM employed a mode-split scheme to solve the governing equations which divided the currents into external and internal modes. The water elevation and vertical averaged velocity were solved by external mode with a smaller time step and the internal mode used the elevation to solve the 3D flow field with a larger time step. The external time step and internal time step for the large domain were 1 and 10 s and, for the subdomain, 0.2 and 2 s. Ten sigma layers were employed in the simulation.

3.2.4 FVCOM setup for sediment simulation

The sediment transport was only simulated in the subdomain (Fig. 4). The medium diameter of the sediment was fixed at 4 μm. The decision of parameters for sediment is important
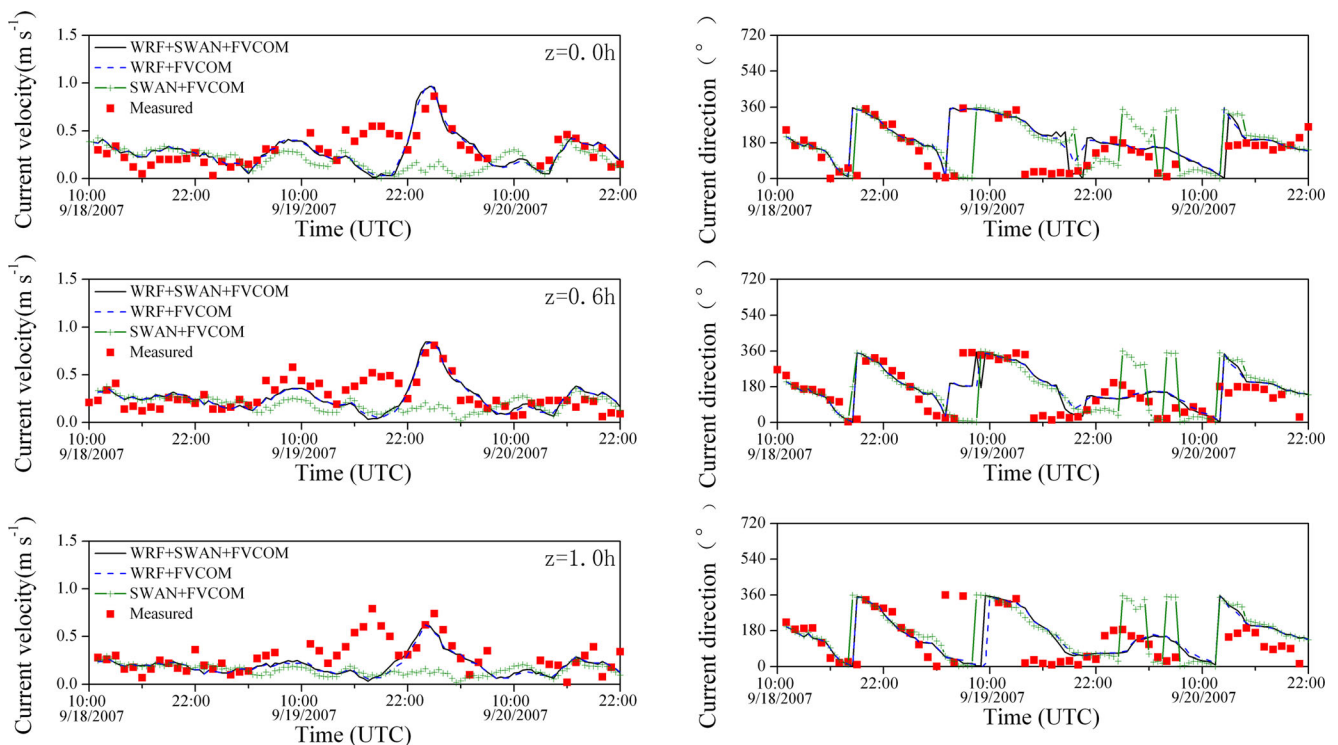

Fig. 15 Time series of simulated current velocities and directions for different model scenarios and the comparison with measured data during Typhoon Wipha at station B

Table 3 Mean absolute error of hydrodynamic results

| Item	Scenario	Mean absolute error
Water elevation	WRF+FVCOM	0.61
	SWAN+FVCOM	0.61
	WRF+FVCOM+SWAN	0.62
Current velocity (surface)	WRF+FVCOM	0.12
	SWAN+FVCOM	0.19
	WRF+FVCOM+SWAN	0.13
Current velocity (0.6 h)	WRF+FVCOM	0.11
	SWAN+FVCOM	0.16
	WRF+FVCOM+SWAN	0.12
Current velocity (bottom)	WRF+FVCOM	0.13
	SWAN+FVCOM	0.18
	WRF+FVCOM+SWAN	0.13
Current direction (surface)	WRF+FVCOM	72.55
	SWAN+FVCOM	89.13
	WRF+FVCOM+SWAN	70.44
Current direction (0.6 h)	WRF+FVCOM	69.56
	SWAN+FVCOM	89.59
	WRF+FVCOM+SWAN	70.51
Current direction (bottom)	WRF+FVCOM	83.56
	SWAN+FVCOM	99.60
	WRF+FVCOM+SWAN	83.31

for the simulation. In the previous research of Xie et al. (2010), who had simulated sediment transport in Lianyungang Harbor, the critical shear stress for erosion was set in the range of 0.1 to 1.2 Nm^{-2}, and the critical shear stress for deposition varied from 0.05 to 0.12 Nm^{-2}. In the present study, the critical shear stress for erosion and deposition were calibrated at 1.2 and 0.07 Nm^{-2}, respectively. Mitchener et al. (1996) found erosion rate varied between 0.0002 and 0.0006 kg m^{-2} s^{-1} according to experiment results on various cohesive muds. Here the erosion rate was calibrated as 0.0004 kg m^{-2} s^{-1}. The parameters for settling velocity were set as follows: The concentration for hindered settling C_{HS} was set to 2.5 kg m^{-3} referring to the work of van Rijn (1987) and the gelling concentration C_{gel} was set to 250 kg m^{-3} according to van Rijn (2007). The nonlinear effects factor m was set to 2 (Dankers and Winterwerp 2007). For the consolidation model, the initial mud solids volume fraction at the surface was 0.0154 assuming a minimum fluid mud density of 1050 kg m^{-3}, and the equilibrium profile predicted by Sanford (2008) was used. The consolidation rate was set to 0.9 day^{-1} which was found to be an optimal value by Sanford (2008). The swelling rate was much smaller than the consolidation rate and was set as $r_s=0.01r_c$ (Sanford 2008; Gong and Shen 2009).

3.3 Results and discussion

The simulation duration was from September 17th to 21st, 2007. The effect of wave-current interaction was included in the subdomain. Simulated results of wind, wave, current, and sediment were compared to the measured data to demonstrate the capability of the integrated model. The measured data was obtained from the stations shown in Fig. 2. Wind speeds and directions were obtained from station A. Stations B and C provided wave parameters and sediment concentration data. Station B also provided measured current data.

Fig. 16 Comparison of water elevation with and without the influence of waves during Typhoon Wipha at locations with water depth of −1 and +1 m
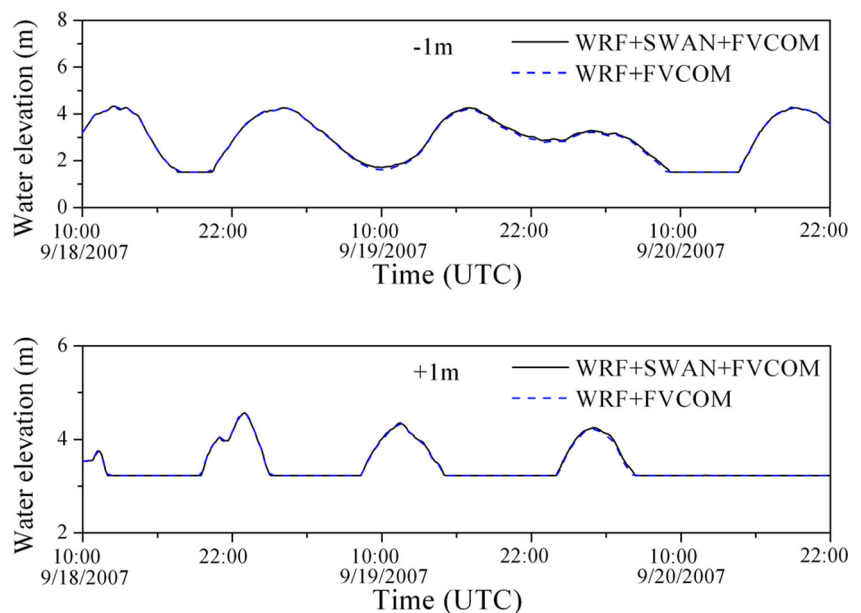
3.3.1 Atmosphere results

Wind fields play an important role in the simulation of waves and hydrodynamic and, as a result, affect the simulation of sediment transport. Simulated wind speed and direction with and without assimilation were compared with measured data obtained at station A. The simulation results were also compared with the QSCAT/NCEP blended ocean winds data (http://dss.ucar.edu/datasets/ds744.4/), as shown in Figs. 5 and 6. The mean absolute errors were calculated and presented in Table 1. The simulation results with assimilation show the best agreement with the measured data both in plots and mean absolute errors, compared with the other two scenarios. It is shown that the wind speed increased as Wipha approaches Lianyungang Harbor, reached over 20 ms^{-1} at about 14:00 of September 19th (UTC) and diminished after several hours. A slight underestimation occurred from about 4:00 to 12:00 of September 19th (UTC). The peak wind was achieved at about 18:00 of September 19th (UTC) when the center of the typhoon reached Lianyungang Harbor (shown as Fig. 7). The simulated track by the WRF model was shown and compared to the observed track (http://www.wztf121.com/). It could be demonstrated that the simulated track by WRF was in

accordance with the observation. For QSCAT/NCEP data, it underestimated the peak of wind speed during Wipha, only reaching 17.5 ms^{-1}. But the QSCAT/NCEP overestimated during low wind speeds. In general, the WRF results could better reproduce the wind directions at station A, compared to the QSCAT/NCEP data, shown in Fig. 7. It was demonstrated that the QSCAT/NCEP data could not reproduce the sharp change of wind fields in the extreme events such as typhoon. It was probably because the temporal and spatial resolutions of the QSCAT/NCEP data were 6 h and 0.5°, respectively, which were not enough to describe the wind fields of the typhoon. For example, the peak wind might be skipped due to the large temporal resolution. The simulation of the WRF model, as described in Section 3.2.1, had a grid resolution of 15 km and a time step of 90 s for the large domain and a grid resolution of 5 km and a time step of 30 s for the subdomain simulation. The WRF and QSCAT/NCEP wind fields for the large domain of the Atmosphere model at 18:00 of September 19th (UTC), when the peak wind occurred, were compared in Fig. 8. Wind fields at 12:00 of September 20th (UTC) were also presented in Fig. 8 to provide more evidence. At 18:00 of September 19th (UTC), the vortex of the typhoon obtained by the WRF model in the Yellow Sea is near Lianyungang Harbor and at the mainland in the south of Lianyungang

Fig. 17 Time series of simulated sediment concentration for different model scenarios and the comparison with measured data during Typhoon Wipha at station B
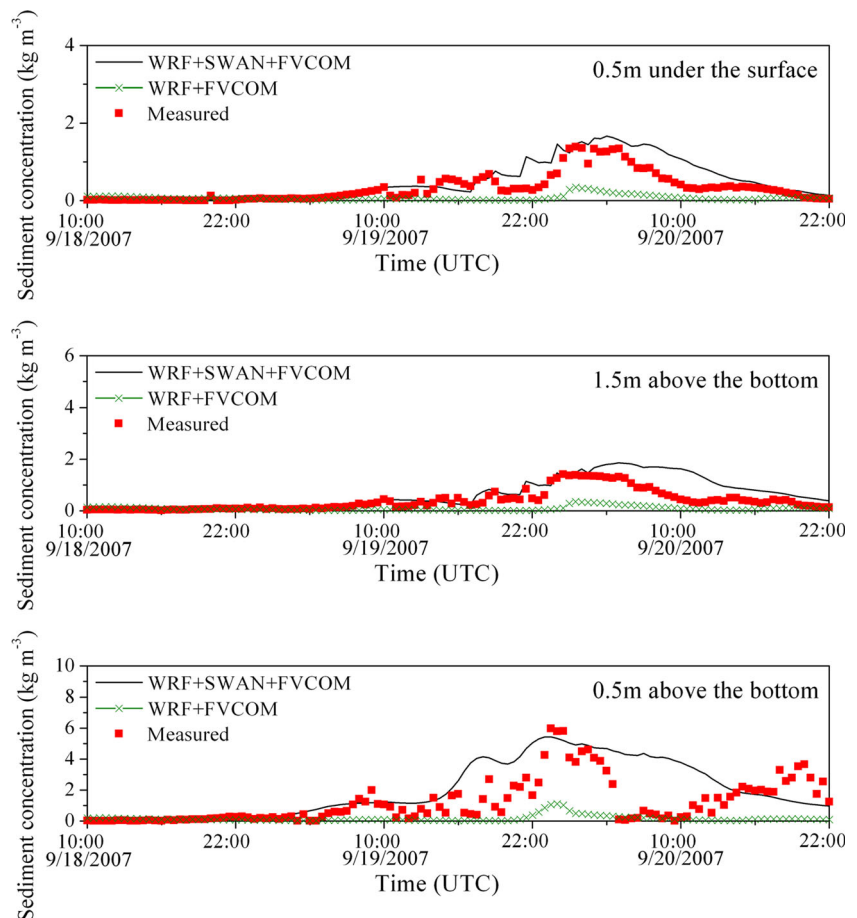
Harbor, while no vortex was found in QSCAT/NCEP wind field. At 12:00 of September 20th (UTC), for the wind field of the WRF model, a vortex was formed on the track of the typhoon, in the Yellow Sea at the east of Lianyungang Harbor. For the QSCAT/NCEP wind field, there was a vortex at the mainland in the north of Lianyungang Harbor. Though the QSCAT/NCEP data did form a vortex, it still could be demonstrated that the cyclone style of the typhoon field was reproduced better by the WRF model, especially at the sea area of Lianyungang Harbor. WRF showed good performance in the simulation of both intensity and track of the typhoon.

3.3.2 Wave results

Simulated significant wave heights and mean wave periods were compared with observed data at station B and station C, shown in Figs. 9 and 10. Wave direction data were available only at station B and comparison of simulation and measurements was shown in Fig. 11. The mean absolute errors were shown in Table 2. The integrated model simulated waves affected by water elevation and flow field (WRF+FVCOM+SWAN). Wave results without the influence of water elevation and flow field (WRF+SWAN) are also shown. It was

demonstrated that wave height increased slightly at high water level and decreased due to the decline of water elevation. But there was no apparent influence of tide on wave period and direction. The mean absolute errors also showed little difference between two cases, see Table 2. The peak wave height was reached at about 19:00 of September 19th (UTC), which lagged the time of peak wind for 1 h, and the wave vector field of the integrated model in the large domain was shown in Fig. 12. The wave vector field simulated by QSCAT/ NCEP wind data was also presented. Corresponding to the wind fields in Fig. 8, we further presented the wave vector fields driven by WRF and QSCAT/NCEP wind field at 13:00 September 20th (UTC), which lagged the time of wind fields for 1 h. Wave driven by WRF wind field propagated anticlockwise due to the cyclone style motion of the wind at the center of the typhoon, and especially at 13:00 of September 20th (UTC), a vortex was formed clearly in the Yellow Sea in accordance with the wind vortex, while the wave field simulated with QSCAT/NCEP data did not show vortex. The influence of wind on wave field was more reasonably reproduced by the integrated model. The wind played such an important role that the accuracy of wind fields to some degree determined the results of wave field and

Fig. 18 Time series of simulated sediment concentration for different model scenarios and the comparison with measured data during Typhoon Wipha at station C
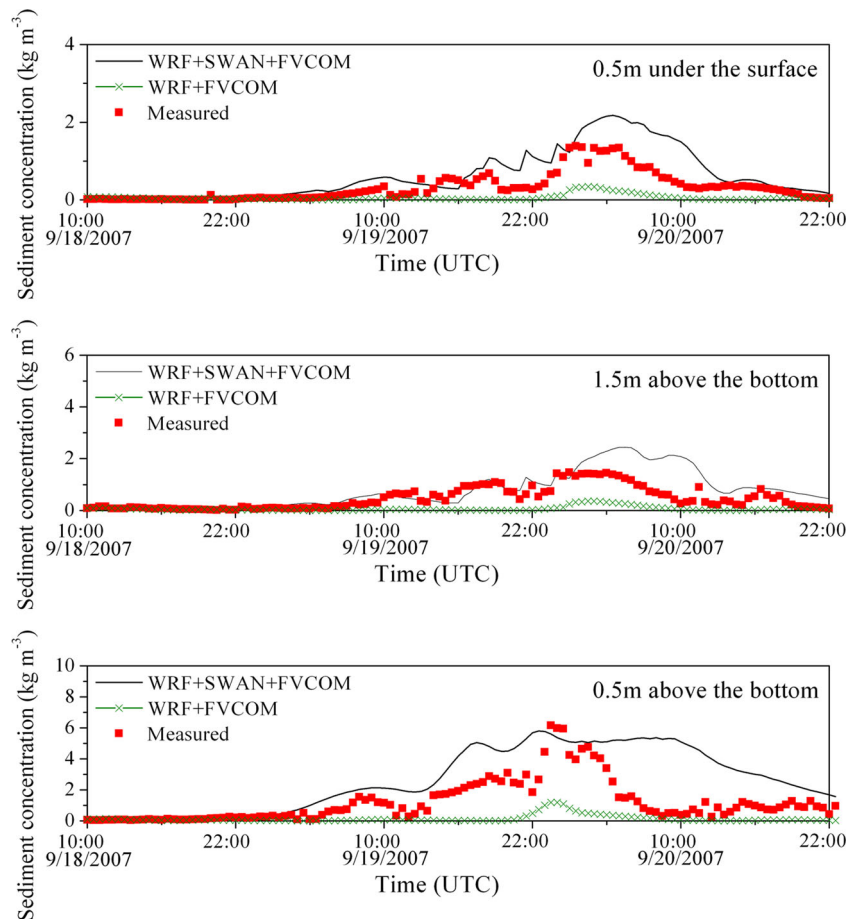
affected sediment transport in the further simulation. Wave period was overestimated in the last day at station B and underestimated in the first day at station C.

Though the difference between waves with and without the influence of tide is not apparent, shown in Figs. 9, 10, and 11, the difference between significant wave heights at station C is larger than B because the water at station C is shallower. It is anticipated that the influence will become more apparent approaching the coastline. So we selected a location near station C with a water depth of −1 m (119° 32 E, 36° 37 N) and compared the simulated wave heights with and without the influence of tide in Fig. 13. The influence is much more apparent. The wave height obtained by WRF+FVCOM+SWAN fluctuated obviously, and it could reach 1 m at high water elevation and decrease to about 0 m due to wave breaking at shallow water as the water elevation declined. But the significant wave height by WRF+SWAN maintained the value of 0.6 m, which was probably because the water kept a shallow depth and only the broken wave height was obtained. So during the simulation at Lianyungang Harbor, the tide variation greatly affected nearshore waves.

3.3.3 Hydrodynamic results

Hydrodynamic condition is another factor that affects the prediction of sediment transport. The radiation stresses induced by waves could affect the current results. Winds could also have influences on currents. To investigate the influences of waves and winds, simulation results of current including the influence of winds and waves (WRF+SWAN+FVCOM), without the influence of waves (WRF+FVCOM) and without the influence of winds (SWAN+FVCOM), are compared with measured data at station B. The water elevation was presented in Fig. 14 and the current velocity and direction were shown in Fig. 15. The mean absolute errors were shown in Table 3. Water surface level of SWAN+FVCOM was lower than the other two cases, especially during the time from 16:00 September 19th (UTC) to 6:00 of September 20th (UTC), when strong winds occurred as shown in Section 3.3.1. As for the current speed during the typhoon, wind played a very important role, shown in Fig. 15. The current velocity of SWAN+FVCOM case only reached about 1/3 compared with the other two cases. Current direction also showed inconformity with the measured data during the strong wind period. However, for comparison between WRF+SWAN+FVCOM and WRF+FVCOM cases,

Fig. 19 Time series of simulated sediment concentration for settling velocity calculated by equation and set as fixed values and the comparison with measured data during Typhoon Wipha at station B
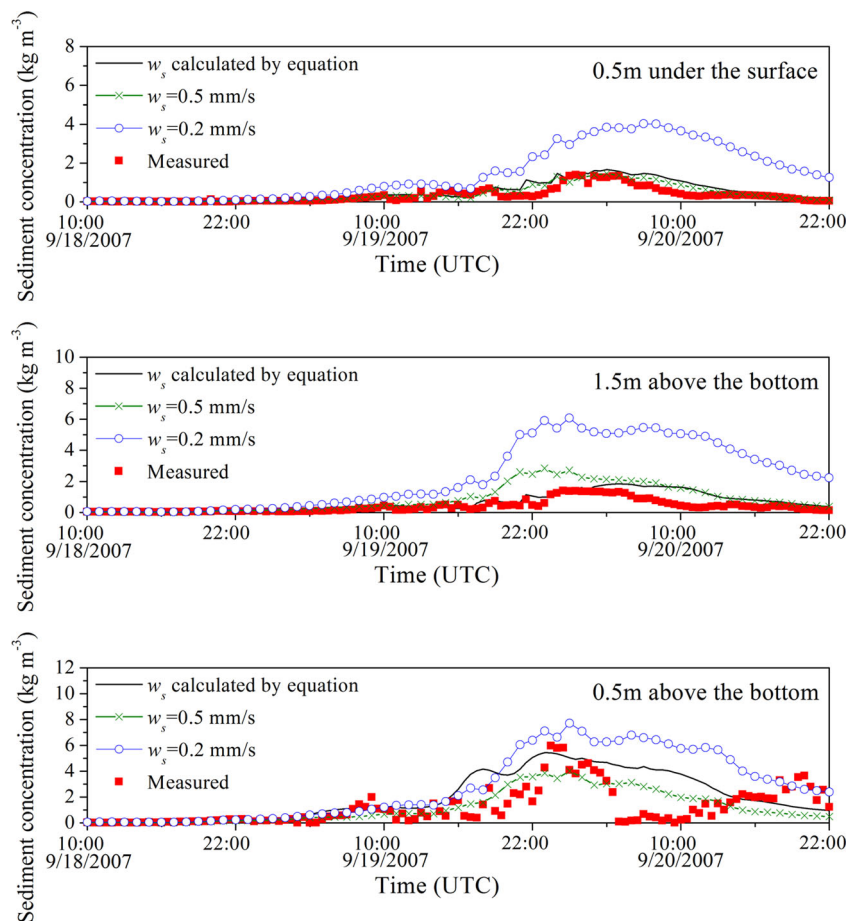
the difference was not apparent. Differences of simulated water elevations at station B of the two cases were only about several centimeters. Similar to the analysis of wave results, the water elevation results for two cases at locations with water depth of −1 m (119° 32 E, 36° 37 N) and +1 m (119° 32 E, 36° 37 N) were also compared and shown in Fig. 16. But the difference of the two cases was still small, which demonstrated that during typhoon processes, the influence of wave on current was not apparent around Lianyungang Harbor. The effects of wave-induced radiation stresses were probably weakened due to the small slope of the beach. The same phenomenon had been found by a previous work of Yu (2010). Therefore, the wind played a more important role that affected the water elevation and current in Lianyungang Harbor during Typhoon Wipha.

From the results of the WRF+SWAN+FVCOM case, it was shown that water surface level increases slightly at about 16:00 of September 19th (UTC) due to the increase of wind speed. At about 4:00 of September 20th (UTC), the water level decreases. In general, the measured current velocity has three peaks, at about 10:00 and 18:00 of September 19th and 3:00 of September 20th (UTC). The model failed to reproduce the middle peak probably due to the underestimation of the wind speed. Current directions showed reasonable agreement with the measured data.

3.3.4 Sediment results

For cohesive sediment transport, the bottom shear stress is an important factor because it determines the erosion and deposition fluxes which affect the sediment concentration. In storm events, strong waves are always induced and can greatly enhance the bottom shear stress due to the orbital motions near the bottom. The suspended sediment concentrations with (WRF+SWAN+FVCOM) and without (WRF+FVCOM) the influence of waves were compared with the measured data at station B and station C, respectively, shown in Figs. 17 and 18. In the WRF+FVCOM case, without the wave-induced shear stress, only a few sediments were suspended into the water, so the sediment concentration was very small, with the maximum bottom concentration of 1 kg m^{-3}. But for the WRF+SWAN+FVCOM case, sediment concentration at different depths showed reasonable agreement with the measured data. With the growth of the typhoon, sediment concentration increased and reached the maximum of 6 kg m^{-3} at about 23:00 of September 19th (UTC).The peak value agreed well with the observations, but overestimation occurred after the peak. This is because an overestimation of wave height occurred around 10:00 of September 20th (Fig. 9), inducing an overestimation of the bed shear stress and consequently an

Fig. 20 Time series of simulated sediment concentration for settling velocity calculated by equation and set as fixed values and the comparison with measured data during Typhoon Wipha at station C
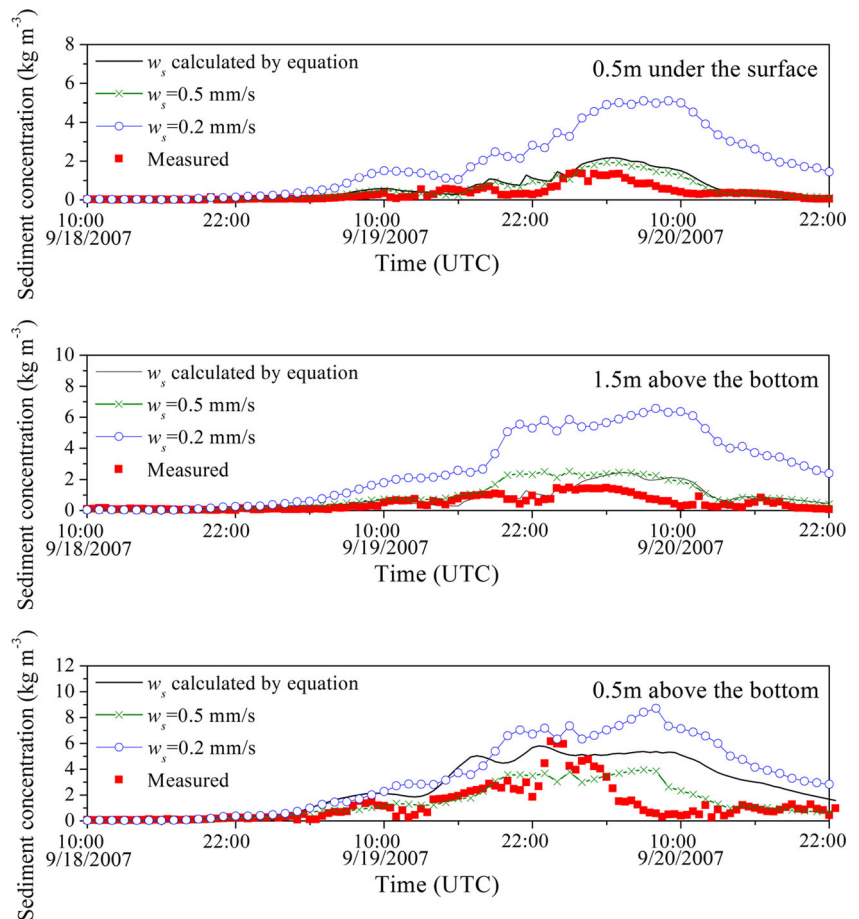
overestimation of the suspended sediment concentration. It could be demonstrated that waves played an important role in the cohesive sediment transport during storm processes.

Simulated concentrations with settling velocity calculated by Eq. (16) and set as fixed values are compared with the measured data and shown in Figs. 19 and 20. Mean absolute errors of sediment results are presented in Table 4. For settling velocity set as 0.5 mm s^{-1}, the sediment concentration at 0.5 m under the surface and 1.5 m above the bottom is close to measured data at both station B and station C. At 0.5 m above the bottom, though the mean absolute error is small, the simulated concentration could not reach the peak measured values which makes the simulated results too conservative. While for settling velocity set as 0.2 mm s^{-1}, the simulated concentrations at different depths are all larger than the measured. In general, though the model has the tendency to overestimate the observed sediment concentration, the model with the settling velocity calculated by equation still obtains the most reasonable results.

Figure 21 shows the development of the sediment concentration fields around Lianyungang Harbor for the WRF+ SWAN+FVCOM case at the surface and bottom. The sediment concentration was larger at nearshore area and at the estuary of Guan River (Fig. 2). At about 18:00 of September 18th, 2007 (UTC), Wipha made landfall at Xiaguanzhen of Zhejiang Province (Fig. 3) with a distance of 845 km south from Lianyungang Harbor. The suspended sediment concentration was less than 1 kg m^{-3} except at the Guan River estuary, where the concentration was larger than 2 kg m^{-3}. At that time, the sediment concentration was small because the typhoon was far from Lianyungang Harbor, and the wave height was small. As Typhoon Wipha approached, the sediment concentration increased and the bottom concentration nearshore was around 3–5 kg m^{-3}. The bottom concentration reached to about 6 kg m^{-3} at 23:00 of September 19th (UTC), which lagged the appearance of peak wave (19:00 of September 19th; UTC). After the eye of Typhoon Wipha left from Lianyungang Harbor, the suspended sediment concentration decreased. The bottom concentration decreased to less than 2.4 kg m^{-3} for nearly the whole area at 4:00 of September 21st (UTC).

Vertical profiles of suspended sediment concentration in the typhoon event at station C are shown in Fig. 22. Only the moments shown in Fig. 21 are presented. In general, the surface sediment concentration was not large even during the typhoon process, with the maximum value less than 1 kg m^{-3}. But the bottom sediment concentration increased a lot as the typhoon approached. For example, the bottom sediment concentration at station C increases from 0.1 to 6 kg m^{-3}. High sediment concentration near the bed appeared during Typhoon Wipha.

Deposition in 150,000 DWT approach channel during Typhoon Wipha, shown in Fig. 2, was calculated by the

Table 4 Mean absolute error of sediment results

Item	Scenario	Mean absolute error
Sediment concentration 0.5 m under the surface (station B)	WRF+FVCOM	0.29
	WRF+FVCOM+ SWAN/w_s calculated	0.20
	w_s=0.5 mm s^{-1}	0.14
	w_s=0.2 mm s^{-1}	1.13
Sediment concentration 1.5 m above the bottom (station B)	WRF+FVCOM	0.32
	WRF+FVCOM+ SWAN/w_s calculated	0.27
	w_s=0.5 mm s^{-1}	0.49
	w_s=0.2 mm s^{-1}	1.93
Sediment concentration 0.5 m above the bottom (station B)	WRF+FVCOM	0.29
	WRF+FVCOM+ SWAN/w_s calculated	0.20
	w_s=0.5 mm s^{-1}	0.89
	w_s=0.2 mm s^{-1}	2.45
Sediment concentration 0.5 m under the surface (station C)	WRF+FVCOM	0.28
	WRF+FVCOM+ SWAN/w_s calculated	0.32
	w_s=0.5 mm s^{-1}	0.23
	w_s=0.2 mm s^{-1}	1.54
Sediment concentration 1.5 m above the bottom (station C)	WRF+FVCOM	0.40
	WRF+FVCOM+ SWAN/w_s calculated	0.36
	w_s=0.5 mm s^{-1}	0.51
	w_s=0.2 mm s^{-1}	2.26
Sediment concentration 0.5 m above the bottom (station C)	WRF+FVCOM	1.08
	WRF+FVCOM+ SWAN/w_s calculated	1.46
	w_s=0.5 mm s^{-1}	0.61
	w_s=0.2 mm s^{-1}	2.21

sediment transport model. The density of the deposited mud was calculated by the consolidation process and set as fixed values, respectively, in the simulation of deposition. Siltation thicknesses of 20 locations (Fig. 23) along the channel are shown in Fig. 24. Measurement of thickness from location 3+0 to 7+0 was carried out during the typhoon, presented in Fig. 24. Considering the consolidation process, the simulated deposition thickness decreased from 0.6 m to smaller than 0.2 m along the channel, which was generally agreed with the measured data. However, the measured maximum thickness was about 0.9 m in the range of 4.5 and 5.5 km distance from location 0+0, but the simulation result only reached half of it. This is because that the bottom elevation of this section is lower, so fluid mud formed in the channel flows toward there. It is realized that a submodel of fluid mud transport needs to be implemented in the cohesive sediment transport model to obtain better results. The simulated average thickness in the channel is about 0.5 m, which is in general agreement with the observations.

Fig. 21 Sediment concentration (kg m^{-3}) around Lianyungang Harbor during Typhoon Wipha (*left*: surface; *right*: bottom)

September 18, 2007 18:00

September 19, 2007 23:00

September 21, 2007 4:00
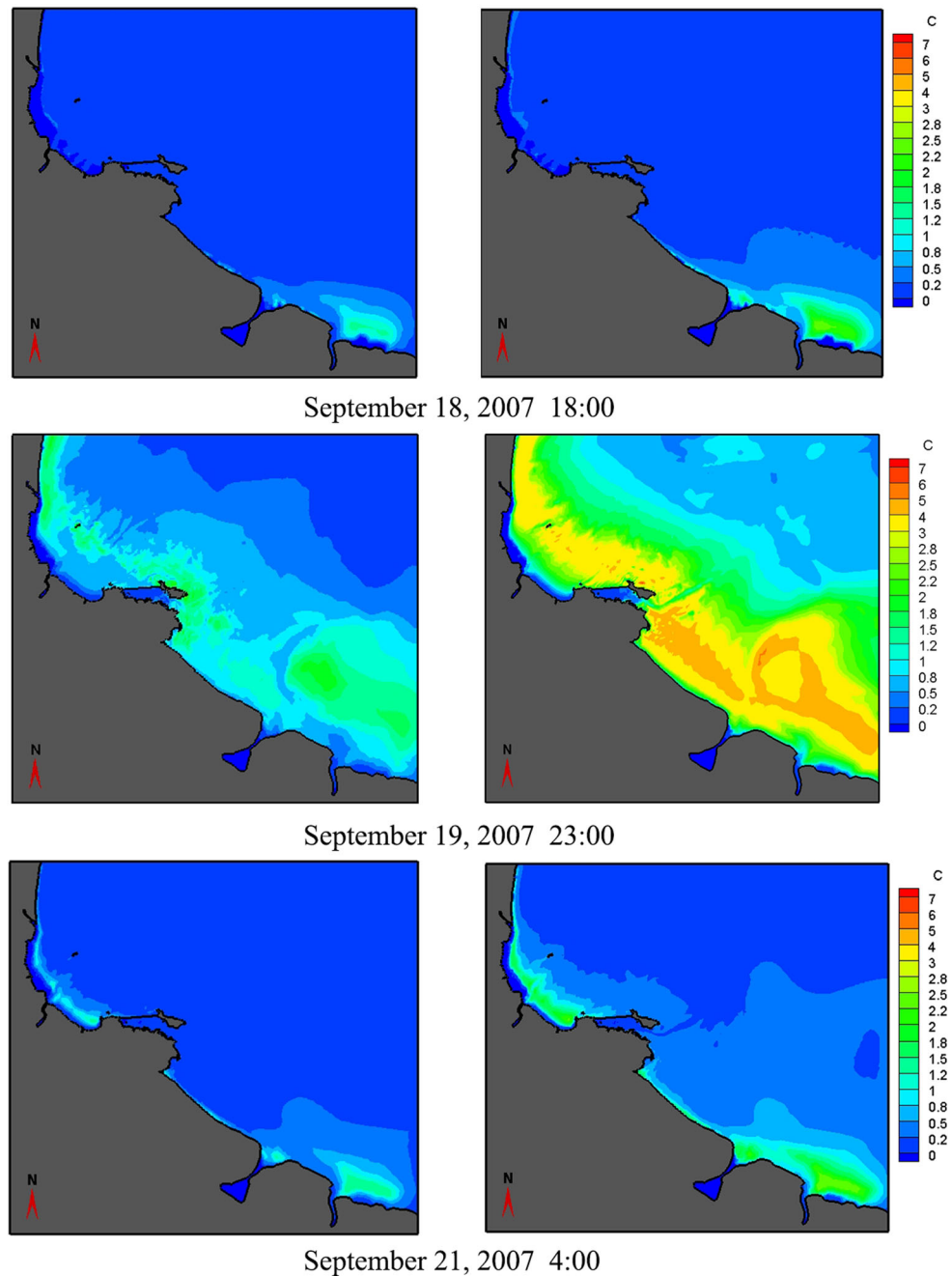
Density profiles of the deposited mud were simulated by the consolidation model. Simulated density profiles at locations 0+0, 2+0, 4+0, and 6+0 are shown in Fig. 25. There were no observations of fluid mud density profiles in the 150,000 DWT approach channel available for validation, but measurement was carried out in a trail channel near the Lianyungang channel after Typhoon Kompasu in 2010 and shown in Fig. 26. Compared to the measured data, the model predictions have the same trend as the measured profile.

4 Conclusions

An integrated atmosphere-wave-3D hydrodynamic and cohesive sediment transport model with unstructured grid has been developed with components of atmosphere model WRF, wave model SWAN, and hydrodynamic and sediment transport model FVCOM. Flocculation and hindered settling for cohesive sediment was included, and a first-order empirical consolidation model was added into the sediment transport model.
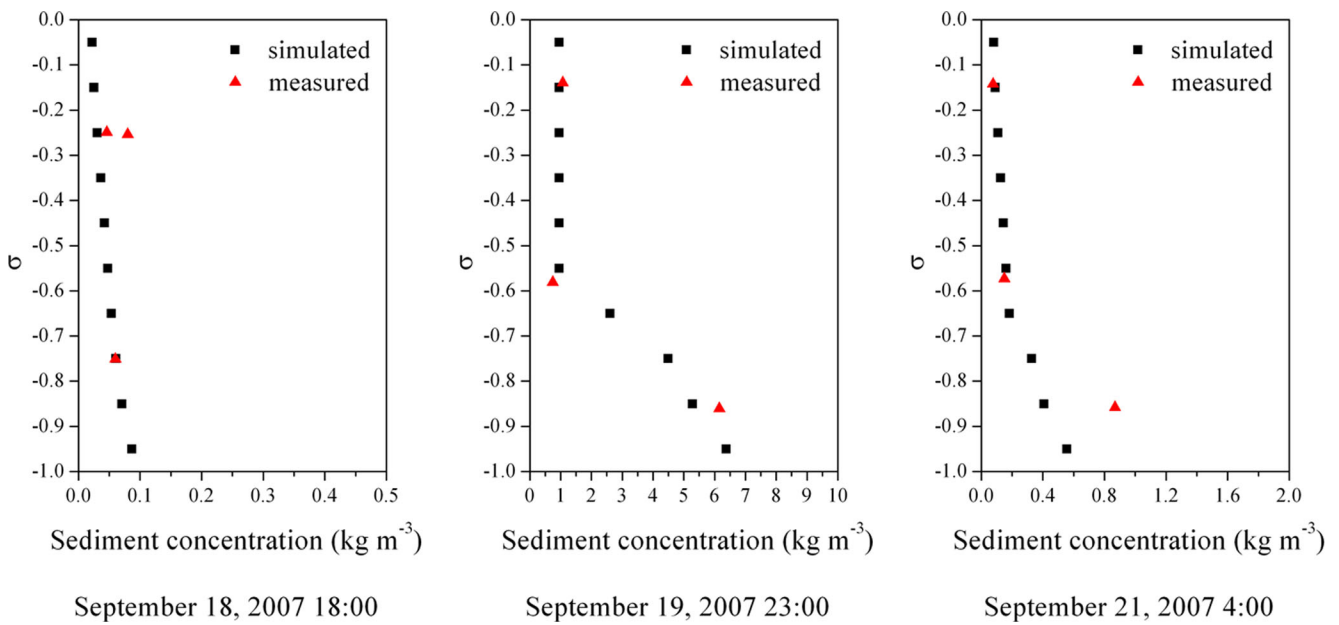
Fig. 22 Vertical profiles of suspended sediment concentration of station C during Typhoon Wipha

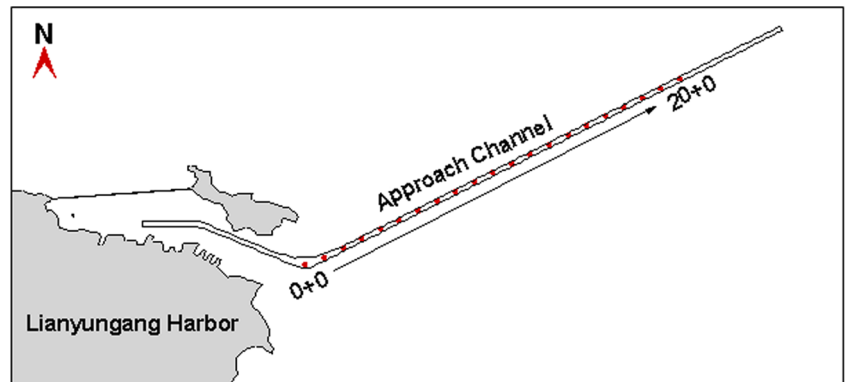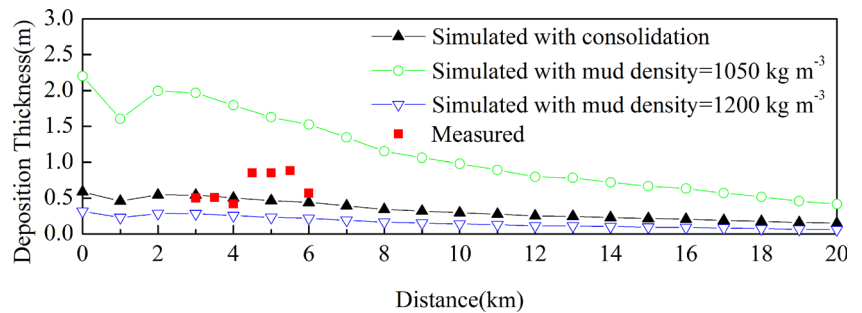Fig. 23 Locations of the 150,000 DWT approach channel and sampling points

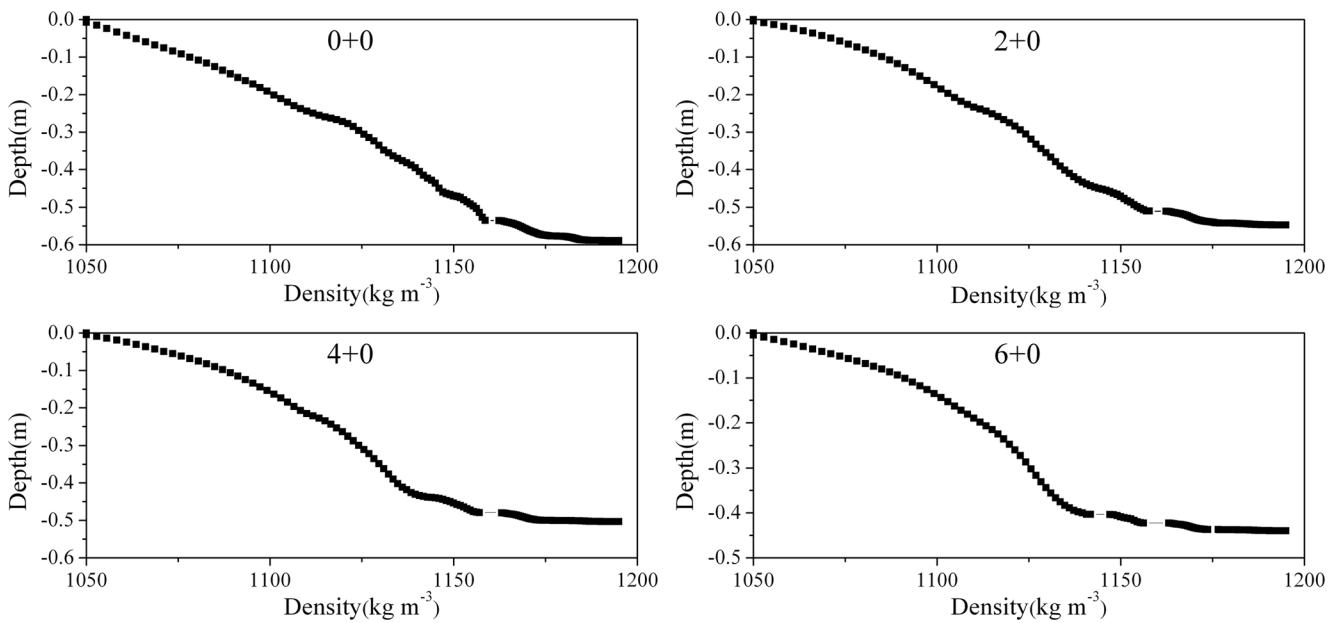Fig. 24 Comparison of simulated and measured siltation thickness along the channel

**Fig. 25** Simulated density profile at locations 0+0, 2+0, 4+0, and 6+0

Data fields were exchanged offline between components to expound their interaction. The atmosphere model WRF provided the wind field for simulation of wave and hydrodynamics. The FVCOM simulated the hydrodynamics with the provided wave field and radiation stress field from the SWAN model. The results of water elevation and flow field were returned to the SWAN model to update the wave results. With the influence of wind field from WRF and the updated wave field and radiation stress field from the SWAN model, the FVCOM updated the hydrodynamic and simulated the cohesive sediment transport.

The integrated model was applied in Lianyungang Harbor during Typhoon Wipha to investigate the coastal dynamics and cohesive sediment transport in storm events. Simulation results of wind, wave, current, and sediment were obtained and compared to measured data. The effects of components on each other were investigated and some conclusions were obtained.

The QSCAT/NCEP data could not reach the measured peak wind speed during the typhoon process probably due to the low temporal and spatial resolutions. For the same reason, the cyclone style of the wind field of typhoon was better reproduced by the WRF model, compared with QSCAT/NCEP data. The simulation results of wind speeds and directions by WRF with assimilation showed general agreement with the observations.

Wave simulation was driven by winds and affected by tide through water elevation and flow field. Wave vector field showed that the wave results were affected directly by the wind field, with an obvious wave vortex appearing in accordance with the wind vortex. The magnitudes of wave heights, mean wave periods, and wave directions were in reasonable agreement with the measured data. The influence of water elevation and flow field was more apparent as the water got shallower. The propagation of wave was in accordance with the wind field, with the peak wave height appearing near the center of the typhoon wind field.

Fig. 26 Measured density profile in the trail channel
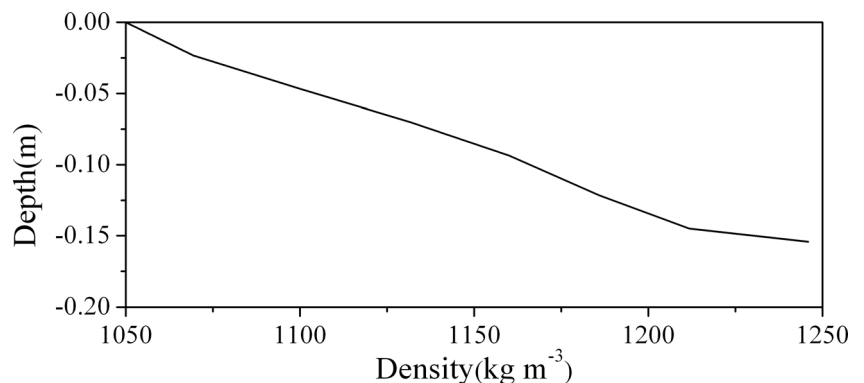
Hydrodynamic modeling took account of the influence of winds and waves. Waves affected the current through radiation stress. In the Lianyungang Harbor, the influence was found not apparent even at the location with a water depth of −1 m, with only a difference of several centimeters between water elevations with and without the influence of wave. The wind played an important role in the simulation of current speed.

The cohesive sediment transport was simulated under the effects of wind, wave, and current. Waves played a dominant role through the wave-induced shear stress which to some degree determined the erosion and deposition fluxes. In general, the sediment results of concentration, siltation thickness, and density profiles compared well with the observations. However, the modeling of siltation in the channels failed to predict the actual value due to the flow of fluid mud. A fluid mud transport model needs to be developed and implemented into the present model.

For the cohesive sediment transport during storm events, the factors of wind, current, and wave all played important roles. The integrated model we have developed could solve the problems of cohesive sediment transport simulation in storm events for the reason that it could provide high-resolution atmosphere forcing for wave, current, and sediment transport simulation and it could also reproduce the complex processes of the hydrodynamics and sediment transport and the interactions between them. Furthermore, it included some specific processes of settling and consolidation for cohesive sediment. Therefore, the integrated model is necessary for the prediction of sediment transport during storm processes. More processes concerning the cohesive sediment and the fluid mud flow model will be carried out with future effort.

References

Ariathurai R, Arulanandan K (1978) Erosion rates of cohesive soils. J Hydraul Div 104(2):279–283

Booij N, Ris RC, Holthuijsen LH (1999) A third-generation wave model for coastal regions. Part I: model description and validation. J Geophys Res 104(C4):7649–7666

Burchard H (2002) Applied turbulence modeling in marine waters. Springer, Berlin, p p229

Chen DC, Yu ZY, Jin L, Zhang QS (1994) Hydrodynamic characteristics, sediments and environment problems on the muddy coast in the construction of Lianyungang deep water harbor. J East China Normal Univ (Natural Science) 4:77–84 (in Chinese)

Chen CS, Liu HD, Beardsley RC (2003) An unstructured grid, finite-volume, three-dimensional, primitive equation ocean model: application to coastal ocean and estuaries. J Atmos Ocean Technol 20:159–186

Chen CS, Zhu JR, Zheng LY, Ralph E, Budd JW (2004) A non-orthogonal primitive equation coastal ocean circulation model: application to Lake Superior. J Great Lakes Res 30(1):41–54

Chen XJ, Huang H, Chen ZY, Wang XZ (2010) A numerical simulation study on Typhoon Manyi spiral bands. Meteorol Disaster Reduction Res 33(4):9–15 (in Chinese)

Dankers PJT, Winterwerp JC (2007) Hindered settling of mud flocs: theory and validation. Cont Shelf Res 27:1893–1907

Fan EM, Chen SL, Zhang GA (2009) The hydrological and sediment characteristics in Lianyungang coastal waters. World Sci-tech R & D 31(4):703–707 (in Chinese)

Gong WP, Shen J (2009) Response of sediment dynamics in the York River Estuary, USA to tropical cyclone Isabel of 2003. Estuarine, Coastal and Shelf Sci 84(1):61–74

Gu JF, Xiao QN, Kuo YH, Barker DM, Xue JS, Ma XX (2005) Assimilation and simulation of Typhoon Rusa (2002) using the WRF system. Adv Atmos Sci 22(3):425–427

Hamrick JM (1992) A three-dimensional environmental fluid dynamics computer code: theorical and computational aspect. Special report No. 317 in Applied Marine Science and Ocean Engineering

Holland GJ (1980) An analytic model of the wind and pressure profiles in hurricanes. Mon Weather Rev 108(8):1212–1218

Huang JW (1989) An experimental study of the scouring and settling properties of cohesive sediment. Ocean Eng 7(1):61–70 (in Chinese)

Laprise R (1992) The Euler equations of motion with hydrostatic pressure as independent variable. Mon Weather Rev 120(1):197–207

Li MG, Zheng JY (2007) Introduction to Chinatide software for tide prediction in China seas. J Waterway Harbor 28(1):65–68 (in Chinese)

Liu XH, Huang WR (2009) Modeling sediment resuspension and transport induced by storm wind in Apalachicola Bay, USA. Environ Model Softw 24(11):1302–1313

Mellor GL (2003) The three-dimensional current and surface wave equations. J Phys Oceanogr 33:1978–1989

Mellor GL (2005) Some consequences of the three-dimensional current and surface wave equations. J Phys Oceanogr 35:2291–2298

Mellor GL, Blumberg A (2004) Wave breaking and ocean surface layer thermal response. J Phys Oceanogr 34:693–698

Mellor GL, Yamada T (1982) Development of a turbulence closure model for geophysical fluid problems. Rev Geophys 20(4):851–875

Mitchener H, Torfs H, Whitehouse RJS (1996) Erosion of mud/sand mixtures. Coast Eng 29(1–2):1–25

Neves (2003) Mohid description. Technical University of Lisbon, Portugal

Olabarrieta M, Warner JC, Armstrong B, Zambon JB, He R (2012) Ocean–atmosphere dynamics during Hurricane Ida and Nor'Ida: an application of the coupled ocean–atmosphere–wave–sediment transport (COAWST) modeling system. Ocean Model 43–44:112–137

Rosenfeld D, Khain A, Lynn B, Woodley W (2007) Simulation of hurricane response to suppression of warm rain by sub-micron aerosols. Atmos Chem Phys Discuss 7:5647–5674

Sanford LP (2008) Modeling a dynamically varying mixed sediment bed with erosion, deposition, bioturbation, consolidation, and armoring. Comput Geosci 34:1263–1283

Shi Z, Zhou HJ (2004) Controls on effective settling velocities of mud flocs in the Changjiang Estuary, China. Hydrolog Process 18(15):2877–2892

Skamarock WC, Klemp JB, Dudhia J, Gill DO, Barker DM, Duda MG, Huang XY, Wang W, Powers JG (2008) A Description of the advanced research WRF version 3. NCAR Technical Note NCAR/TN-475+STR

Smagorinsky J (1963) General circulation experiments with the primitive equations I. The basic experiment. Mon Weather Rev 91(3):99–164

Styles R, Glenn SM (2000) Modeling stratified wave and current bottom boundary layers on the continental shelf. J Geophys Res 105(C10): 24119–24139

Svendsen IA (1984) Wave heights and set-up in a surf zone. Coast Eng 8(4):303–329

Thorn MFC (1981) Physical processes of siltation in tidal channels. Proc Hydraulic Modeling of Maritime Engineering Problems, Institution of Civil Engineers, London, pp 47–55

van Rijn LC (1987) Mathematical modeling of morphological processes in the case of suspended sediment transport. Communication No. 382, Delft Hydraulic Laboratory, Delft, the Netherlands

van Rijn LC (2007) Unified view of sediment transport by current and waves II: suspended transport. J Hydraul Eng 133(6):668–689

Vinzon SB, Mehta AJ (2003) Lutoclines in high concentration estuaries: Some observations at the mouth of the Amazon. J Coastal Res 19(2): 243–253

Wang BC, Yu ZY, Liu CY, Jin QX (1980) The change of coasts and beaches and the movement of longshore sediments of Haizhou Bay. Acta Oceanol Sin 2(1):79–96 (in Chinese)

Wang W, Bruyère C, Duda M, Dudhia J, Gill D, Lin HC, Michalakes J, Rizvi S, Zhang X (2011) ARW version 3 modeling system user's guide. Mesoscale and Microscale Meteorology Division, National Center for Atmosphere Research

Warner JC, Butman B, Dalyander PS (2008a) Storm-driven sediment transport in Massachusetts Bay. Cont Shelf Res 28:257–282

Warner JC, Sherwood CR, Signell RP, Harris CK, Arango HG (2008b) Development of a three-dimensional, regional, coupled wave, current, and sediment-transport model. Comput Geosci 34:1284–1306

Warner JC, Armstrong B, He R, Zambon JB (2010) Development of a coupled ocean-atmosphere-wave-sediment transport (COAWST) modeling system. Ocean Modeling 35:230–244

Xie MX, Zhang W, Guo WJ (2010) A validation concept for cohesive sediment transport model and application on Lianyungang Harbor, China. Coast Eng 57(6):585–596

Yu L (2010) The three-dimensional numerical model of storm surge of Bohai Bay incorporating wave-current coupling. Master thesis, Tianjin University, Tianjin, China, 74pp (in Chinese)

Zhang N (2004) 3D numerical simulation of cohesive sediment transport under winds and waves. Master thesis, Tianjin University, Tianjin, China, 61pp (in Chinese)

Zhao Q (2008) Modeling cohesive sediment siltation in a storm event using an integrated three-dimensional model. 31th International Conference on Coastal Engineering (ICCE2008), pp 2842–2851

Zijlema M (2010) Computation of wind-wave spectra in coastal waters with SWAN on unstructured grids. Coast Eng 57(3):267–277